Nearly inviscid Faraday waves in containers with broken symmetry

M Higuera , E Knobloch and J M Vega

E.T.S.I. Aeronáuticos, Universidad Politécnica de Madrid, Plaza Cardenal Cisneros 3, 28040 Madrid, SPAIN,

Department of Physics, University of California, Berkeley, CA 94720, USA

Abstract. In the weakly inviscid regime parametrically driven surface gravity-capillary waves generate oscillatory viscous boundary layers along the container walls and the free surface. Through nonlinear rectification these generate Reynolds stresses which drive a streaming flow in the nominally inviscid bulk; this flow in turn advects the waves responsible for the boundary layers. The resulting system is described by amplitude equations coupled to a Navier-Stokes-like equation for the bulk streaming flow, with boundary conditions obtained by matching to the boundary layers, and represents a novel type of pattern-forming system.

The coupling to the streaming flow is responsible for various types of drift instabilities of standing waves, and in appropriate regimes can lead to the presence of relaxations oscillations. These are present because in the nearly inviscid regime the streaming flow decays much more slowly than the waves. Two model systems, obtained by projection of the Navier-Stokes-like equation onto the slowest mode of the domain, are examined to clarify the origin of this behavior. In the first the domain is an elliptically distorted cylinder while in the second it is an almost square rectangle. In both cases the forced symmetry breaking results in a nonlinear competition between two nearly degenerate oscillatory modes. This interaction destabilizes standing waves at small amplitudes and amplifies the role played by the streaming flow. In both systems the coupling to the streaming flow triggered by these instabilities leads to slow drifts along slow manifolds of fixed points or periodic orbits of the fast system, and generates behavior that resembles bursting in excitable systems. The results are compared to experiments.

1. Introduction

In recent work on parametrically driven Faraday waves we have shown that in the presence of small viscosity ($C_g \equiv \nu(gh^3 \mid Th/\rho)^{-1/2} \ll 1$) the waves couple to a streaming flow driven in oscillatory viscous boundary layers at rigid walls and the free surface [21]. This flow in turn advects the waves responsible for the oscillatory boundary layers. While the detailed description of this feedback loop (and the derivation of the asymptotically exact equations) is involved, it is known [14, 21] that this coupling is responsible for different types of drift instabilities of the waves, instabilities that have been observed in experiments in annular containers [3] but are absent from the theory when the coupling to the streaming flow is neglected. Subsequent work by Higuera, Vega and Knobloch ([8]) pointed out that the influence of the streaming flow is greatly enhanced for Faraday waves that are not of standing wave type, and derived the equations describing the coupling between the waves and the streaming flow that results. It turns out that the simplest way to destabilize standing waves is to perturb the shape of the container from one of high symmetry to one of lower symmetry. Such a perturbation produces a competition between almost degenerate modes, and introduces secondary

bifurcations into the system that destabilize the primary standing waves already at small amplitude. The dynamics that result can be described by weakly nonlinear theory. Of particular interest is the presence of relaxation oscillations in this regime that resemble the 'bursters' studied in the context of pancreatic β-cells or models of firing neurons. Relaxation oscillations of this type are unusual in fluid mechanics [2], and this alone makes the nearly inviscid Faraday system of great interest.

In this paper we describe two examples for this behavior. We consider first an elliptical container of almost circular cross-section, and summarize the main results obtained from a careful study of a system of model equations derived from the coupled amplitude-streaming flow equations in a particular asymptotic limit. These results indicate that the presence of relaxation oscillations in this system can be attributed to the disparity between the decay times of free surface gravity-capillary waves and the streaming flow that prevails in the nearly inviscid regime. A related study, of a rectangular container of almost square cross-section, also reveals relaxation oscillations, but this time it is possible to relate the results to experiments [19]. Some of our results have been published elsewhere [6].

2. Cylindrical domain

The equations derived in [8] for nearly inviscid Faraday waves in an almost circular domain are

$$A'_{\pm}(\tau) \qquad -(1+i\Gamma)A_{\pm} + i\Lambda A_{\mp} + i\mu\bar{A}_{\mp} + i(\alpha_1|A_{\pm}|^2 + \alpha_2|A_{\mp}|^2)A_{\pm}$$
$$\mp i\Omega \int_{-1}^{0}\int_{0}^{2\pi}\int_{0}^{R} g(r,z)\mathbf{u}\cdot\mathbf{e}_\theta r\,dr\,d\theta\,dz\,A_{\pm}, \tag{1}$$

$$\partial\mathbf{u}/\partial\tau - \qquad [\mathbf{u} + \mathbf{G}(|A_+|,|A_-|)]\times(\nabla\times\mathbf{u}) \qquad -\nabla p + Re^{-1}\Delta\mathbf{u}, \tag{2}$$

where $A_\pm$ are the (complex) amplitudes of clockwise and counterclockwise rotating waves and $\mathbf{u}$ denotes the (incompressible) streaming flow ($\nabla\cdot\mathbf{u}=0$). In these equations Ω is a known constant, and the quantities Γ, Λ and μ are proportional to the detuning, the ellipticity of the container and the forcing amplitude, respectively. The detuning takes into account the mismatch between half the forcing frequency and the natural frequency of inviscid oscillations, and includes the frequency shift due to viscosity, while Λ is proportional to the frequency difference $\omega_1-\omega_2$ between inviscid oscillations along the two principal axes of the container. The time has been scaled by the viscous damping time for a cylinder of height h, viz. $\delta \equiv \gamma_1 C_g^{1/2} + \gamma_2 C_g$, where $C_g \equiv \nu(gh^3+Th/\rho)^{-1/2} \ll 1$, and γ_1 and γ_2 are known constants that depend on the excited mode. Here T denotes the surface tension, ρ is the fluid density, and ν is the kinematic viscosity. This scaling is responsible for the appearance of the Reynolds number

$$Re = (\gamma_1 C_g^{1/2} + \gamma_2 C_g)/C_g \tag{3}$$

in the Navier-Stokes-like equation (2) for the streaming flow. Like all other quantities in these equations the Reynolds number is formally of order one [13, 21], but can in fact be both large and small. For example, if the container is not deep the damping of the waves is dominated by the Stokes boundary layers and $Re \sim \gamma_1/\sqrt{C_g}$, while in a deep container both terms (i.e., $\gamma_1 C_g^{1/2}$ | $\gamma_2 C_g$) contribute to the damping. Calculations show that for the first few modes $\gamma_2/\gamma_1 \sim 10^2$ [13] so that systems with $C_g \lesssim 10^{-4}$, such as water or silicon oils in centimeter-deep containers, have Reynolds numbers $Re \quad O(1/\sqrt{C_g})$. In these systems, therefore, the streaming is only weakly damped and hence is easily driven by time-averaged Reynolds stresses.

Equation (2) also contains a Stokes drift term $\mathbf{G}(A_+, A_-)$ given by

$$\mathbf{G} = (|A_-|^2 - |A_+|^2)g(r,\theta)\mathbf{e}_\theta,$$

and is to be solved subject to the boundary conditions

$$\mathbf{u} \quad [\varphi_1 A_+ \bar{A}_- e^{2im\theta} + \varphi_2(|A_+|^2 + |A_-|^2)]\mathbf{n}_0 \times \mathbf{e}_\theta + [i\varphi_3 A_+ \bar{A}_- e^{2im\theta} + \varphi_4(|A_-|^2 - |A_+|^2)]\mathbf{e}_\theta + \text{c.c.} \tag{4}$$

at all rigid surfaces (i.e., $r = R$ or $z = -1$), and

$$\mathbf{u} \cdot \mathbf{e}_z = (\partial \mathbf{u}/\partial z) \cdot \mathbf{e}_r = 0, \quad (\partial \mathbf{u}/\partial z) \cdot \mathbf{e}_\theta = \varphi_5(|A_-|^2 - |A_+|^2) \tag{5}$$

at the free surface $z = 0$. Here $\mathbf{n}_0$ denotes the outward unit normal, and R is the aspect ratio of the cylinder. The scalar functions $\varphi_1, \ldots, \varphi_5$ and g appearing in these equations are all real, independent of θ, and computable in terms of the components of the excited inviscid linear mode of the system [8]. For a pinned contact line the coefficients γ_1 and γ_2 in (3) and the corresponding inviscid eigenfunctions have been calculated by Martel, Nicolás and Vega ([13]), while Miles ([15]) has calculated the coefficients α_1 and α_2 of the nonlinear terms for a particular case with a free contact line. For $h = 14.1$cm and $Rh = 9.24$cm we have $\alpha_1 = 0.4$, $\alpha_2 = -2.58$.

It is important to observe that in these equations all coefficients are formally of order one. In particular the forcing of the streaming flow remains finite even in the limit of vanishing viscosity, as originally noted by Schlichting ([17]) and Longuet-Higgins ([12]). The boundary conditions (4), (5) show that its magnitude is in general of order $(|A_+|^2, |A_-|^2)$, and hence of order $\mu - \mu_0$, where μ_0 is the threshold for the onset of the Faraday instability. Note also that a nonvanishing streaming flow is associated even with standing waves ($|A_+| = |A_-|$), although for such waves $\mathbf{u} \cdot \mathbf{e}_\theta$ changes sign under reflection $\theta \to -\theta$ and the last term in Eq. (1) vanishes. Thus for standing waves the streaming flow decouples from the amplitudes, although it may be involved in triggering drift instabilities of such waves.

2.1. Circular cylinder

In a circular cylinder ($\Lambda = 0$) the streaming flow decouples from the equations for the amplitudes. To see this we consider waves with azimuthal wavenumber m, and write

$$A_\pm \quad B_\pm e^{-im\theta_0(\tau)},$$

obtaining

$$B'_\pm(\tau) = -(1 + i\Gamma)B_\pm + i\mu B_\mp + i(\alpha_1|B_\pm|^2 + \alpha_2|B_\mp|^2)B_\pm$$

and

$$\theta'_0(\tau) = (\Omega/m)\int_{-1}^{0}\int_0^{2\pi}\int_0^R g(r,z)\mathbf{u} \cdot \mathbf{e}_\theta r\,dr\,d\theta\,dz. \tag{6}$$

These equations provide the simplest description of nearly inviscid Faraday waves in O(2)-symmetric systems, and all their solutions converge to reflection-symmetric steady states of the form

$$B_\pm = R_0 e^{im\theta_0^0}, \tag{7}$$

i.e., to standing waves, and only the spatial phase θ_0 of these waves couples to the streaming flow. This coupling is described by Eq. (6) together with

$$\partial \mathbf{u}/\partial \tau - \mathbf{u} \times (\nabla \times \mathbf{u}) = -\nabla p + Re^{-1}\Delta \mathbf{u}, \quad \nabla \cdot \mathbf{u} = 0, \tag{8}$$

an equation forced by the boundary conditions

$$\mathbf{u} = 2R_0^2[\varphi_1 \cos[2m(\theta - \theta_0)] + \varphi_2]\mathbf{n}_0 \times \mathbf{e}_\theta - 2R_0^2\varphi_3 \sin[2m(\theta - \theta_0)]\mathbf{e}_\theta \tag{9}$$

on either $r = R$ or $z = -1$, and subject to the additional requirement

$$\mathbf{u} \cdot \mathbf{e}_z = (\partial \mathbf{u}/\partial z) \cdot \mathbf{e}_r = (\partial \mathbf{u}/\partial z) \cdot \mathbf{e}_\theta = 0 \tag{10}$$

at z 0. The (constant) arbitrary phase θ_0^0 appearing in (7) has been eliminated by an appropriate rotation. Eqs. (6), (8)-(10) possess, for all R_0^2, reflection-symmetric steady states of the form $\mathbf{u}$ $\mathbf{u}^s(r, \theta - \theta_0, z)$, θ_0 constant, with $\mathbf{u}^s(r, \theta, z) \cdot \mathbf{e}_\theta$ $-\mathbf{u}^s(r, -\theta, z) \cdot \mathbf{e}_\theta$; note that there is a whole family of such states, obtained by an arbitrary rotation. For small R_0^2 the existence and (orbital) asymptotic stability of these states can be ascertained analytically. It turns out that these states can lose stability at finite R_0 either through a parity-breaking bifurcation giving rise to uniformly drifting spatially uniform standing waves (such as those observed in Faraday experiments in annular containers [3]), or via a symmetry-breaking Hopf bifurcation that produces so-called direction-reversing waves [11]. In the latter case the standing waves drift alternately clockwise and counterclockwise but their mean location remains fixed. Solutions of this type have been found in a two-dimensional Cartesian geometry with periodic boundary conditions, and represent the instability that sets in at smallest amplitude [14]. Neither instability is present if the coupling to the streaming flow is ignored.

2.2. Nearly circular cylinder

As soon as Λ / 0 the symmetry of the problem is reduced to the group D_2 generated by

$$A_\pm \to -A_\pm, \quad \theta \to \theta \mid \pi; \qquad A_+ \leftrightarrow A_-, \quad \theta \to -\theta, \quad \mathbf{u} \cdot \mathbf{e}_\theta \to -\mathbf{u} \cdot \mathbf{e}_\theta,$$

and the streaming flow couples to the amplitudes as well. The description of this coupling becomes simpler when the effective Reynolds number of the streaming flow is small (i.e., $\mu - \mu_0$ is small) for then the non-potential term $\mathbf{u} \times (\nabla \times \mathbf{u})$ in Eq. (2) is negligible. In fact this approximation remains qualitatively useful even for larger Reynolds numbers. The absence of nonlinear terms allows us to isolate the part of the streaming flow velocity that contributes to the nonlocal term in Eq. (1), by decomposing the streaming flow variables as

$$(\mathbf{u}, p) \quad (v(r, z, \tau)\mathbf{e}_\theta, 0) + (\hat{\mathbf{u}}, p),$$

where

$$\int_0^{2\pi} \hat{\mathbf{u}} \cdot \mathbf{e}_\theta \, d\theta \equiv 0. \tag{11}$$

Thus

$$\begin{aligned}
A'_\pm(\tau) &= -(1 \mid i\Gamma)A_\pm \mid i\Lambda A_\mp \mid i\mu A_\mp \mid i(\alpha_1|A_\pm|^2 \mid \alpha_2|A_\mp|^2)A_\pm \\
&\qquad \mp 2\pi i\Omega \int_{-1}^{0} \int_0^R g(r, z)v(r, z, \tau)\, r\, dr dz A_\pm, \\
v_\tau &= Re^{-1}(v_{rr} \mid r^{-1}v_r - r^{-2}v \mid v_{zz}), \quad \text{in} \quad 0 < r < R, \quad -1 < z < 0, \\
v &\quad \text{as } r \to 0, \\
v &\quad \varphi_4(|A_-|^2 - |A_+|^2) \quad \text{on } r \quad R \text{ or } z \quad -1, \\
v_z &\quad \varphi_5(|A_-|^2 - |A_+|^2) \quad \text{on } z \quad 0.
\end{aligned}$$

The axisymmetric part of the streaming flow therefore vanishes for standing waves ($|A_+| = |A_-|$).

Although the above model can be integrated numerically by relatively inexpensive methods we simplify it further by expanding the axisymmetric component of the streaming flow velocity, v, in terms of purely azimuthal hydrodynamic modes. These satisfy the eigenvalue equation

$$\begin{aligned}
&\lambda V = V_{rr} + r^{-1}V_r - r^{-2}V + V_{zz} \quad \text{in} \quad 0 < r < R, \quad -1 < z < 0, \\
&V = 0 \text{ as } r \to 0, \quad V = \varphi_4 \quad \text{on } r = R \text{ or } z = -1, \\
&V_z = \varphi_5 \text{ on } z = 0.
\end{aligned}$$

The eigenvalues λ are all real and negative. If only the first such mode is retained, we obtain

$$\begin{aligned} A'_{\pm}(\tau) &\quad -(1+i\Gamma)A_{\pm} + i\Lambda A_{\mp} + i\mu\bar{A}_{\mp} + i(\alpha_1|A_{\pm}|^2 + \alpha_2|A_{\mp}|^2)A_{\pm} \mp i\gamma v_1 A_{\pm}, \\ v'_1(\tau) &\quad \varepsilon(-v_1 + |A_-|^2 - |A_+|^2), \end{aligned} \tag{12}$$

where $\varepsilon = -\lambda_1 Re^{-1} > 0$, and $\lambda_1 < 0$ is the first purely azimuthal hydrodynamic eigenvalue. In the following we define new variables

$$X = \frac{i}{2}(A_+ - A_-), \quad Y = \frac{1}{2}(A_+ + A_-), \quad v = -\frac{v_1}{2},$$

and rewrite equations (12) in the more useful form

$$\begin{aligned} X' = &\quad -(1+i(\Gamma+\Lambda))X + i((\alpha_1+\alpha_2)|X|^2 + 2\alpha_1|Y|^2)X - i(\alpha_1-\alpha_2)\overline{X}Y^2 + i\mu\overline{X} - 2\gamma vY, \\ Y' = &\quad -(1+i(\Gamma-\Lambda))Y + i((\alpha_1+\alpha_2)|Y|^2 + 2\alpha_1|X|^2)Y - i(\alpha_1-\alpha_2)\overline{Y}X^2 + i\mu\overline{Y} + 2\gamma vX, \\ v' = &\quad \varepsilon(-v + i(\overline{X}Y - X\overline{Y})). \end{aligned} \tag{13}$$

This form of the equations makes it clear not only that the (axisymmetric part of the) streaming flow vanishes if either $X \equiv 0$ or $Y \equiv 0$, i.e., for pure standing waves, but also that both modes must be present in order to drive such a flow.

Equations (13) are equivariant with respect to the group D_2 generated by the two reflections

$$R_1 : (X, Y, v) \to (-X, Y, -v), \quad R_2 : (X, Y, v) \to (X, -Y, -v). \tag{14}$$

As a result there are two types of steady states, the *Pure Modes* ($P_\pm$) given by $P_+ \equiv (0, Y, 0) = (0, R_+ e^{i\phi_+}, 0)$ and $P_- \equiv (X, 0, 0) = (R_- e^{i\phi_-}, 0, 0)$, with P_+ invariant under R_1 and P_- under R_2, and the *Mixed Modes* (M), given by $M \equiv (X, Y, v) \equiv (R_- e^{i\phi_-}, R_+ e^{i\phi_+}, v)$, with no symmetry. These and the associated time-dependent states are described in the following section.

2.3. Results

Equations (13) exhibit remarkable behavior when $\varepsilon \ll 1$, i.e., when the time scale for the decay of the slowest-decaying axisymmetric component of the streaming flow is *long* compared to the decay of (free) surface gravity-capillary waves. In the following we therefore take $\varepsilon \equiv 0.01$, and focus on parameter values $\Gamma \equiv -0.5$, $\Lambda \equiv 0.4$, $\gamma \equiv -0.6$, treating μ as a distinguished bifurcation parameter.

Figure 1 shows the resulting pure mode branches together with their stability properties. Both bifurcate subcritically from the flat state. The P_- branch bifurcates first and acquires stability at a saddle-node bifurcation before losing it again at larger amplitude at a symmetry-breaking steady state bifurcation. The P_+ branch is never stable, and neither are the mixed modes connecting the pure mode branches. Thus interesting behavior sets in beyond the symmetry-breaking bifurcation on the P_- branch, i.e., for $\mu > \mu_{SB} \approx 2.8$. In the following we describe the results of numerical integration of Eqs. (13) in this regime.

Once P_- loses stability at SB small perturbations drive the system to a stable branch of R_1R_2-symmetric *periodic orbits*, also shown in Fig. 1. If the corresponding branch is continued backwards (i.e., for $\mu < \mu_{SB}$) one finds that it ultimately terminates in a heteroclinic bifurcation involving the nonsymmetric fixed points $M^\pm$. The eigenvalues of $M^\pm$ at this bifurcation are 0.001940, -0.42229, $-0.998 \pm 4.819i$ and -1.58926 and hence no chaotic dynamics result. An entirely different scenario unfolds when this periodic branch is continued for $\mu > \mu_{SB}$. First, the R_1R_2-symmetric branch undergoes a pitchfork bifurcation that generates a pair of stable asymmetric periodic orbits (see Fig. 1, inset). With further increase in μ these asymmetric orbits undergo a period-doubling bifurcation PD and, as shown in the bifurcation diagram of Fig. 2, chaotic dynamics are found not long after. The chaotic behavior is marked by a *crisis* in which two asymmetric chaotic attractors

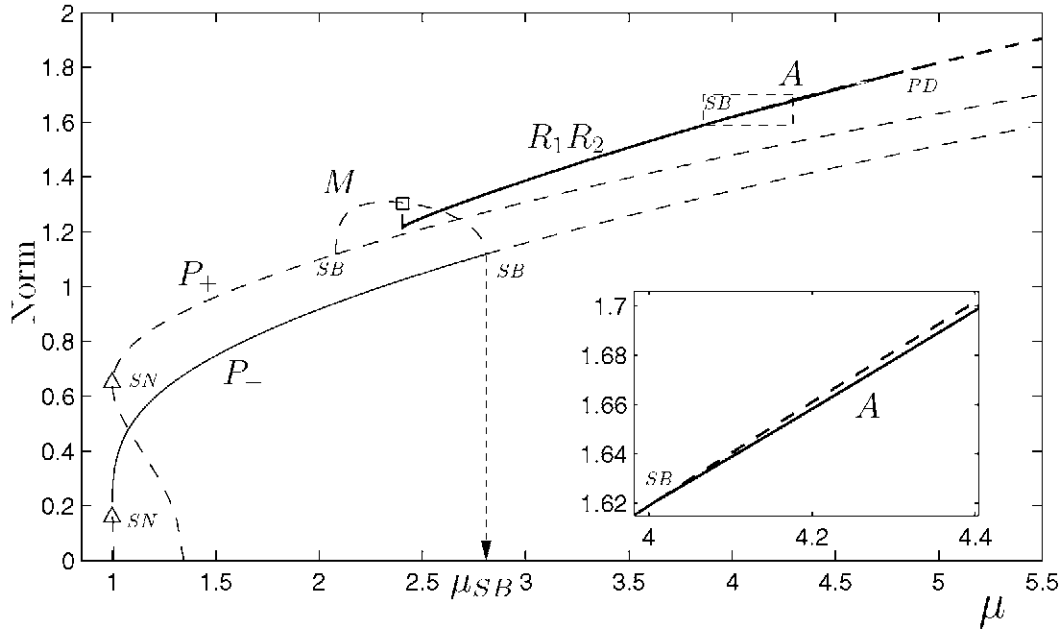

Figure 1. Bifurcation diagram for steady and periodic orbits, in term of Euclidean norm $||(X,Y,v)||$ and L_2 norm $||(X,Y,v)||_{L_2}$, respectively, as a function of μ. Thick solid (dashed) lines correspond to stable (unstable) periodic orbits; thin solid (dashed) lines correspond to stable (unstable) steady states. The arrow indicates the location of a subcritical bifurcation on P_- to unstable M. This bifurcation produces a hysteretic transition to stable R_1R_2-symmetric oscillations that exist between the heteroclinic bifurcation indicated by the symbol $\square$ and a symmetry-breaking bifurcation labeled SB (inset).

collide at $\mu \approx 4.903$ and merge, forming a symmetric chaotic attractor (a symmetry-increasing bifurcation). The interval over which chaos is observed is relatively short ($4.902 \lesssim \mu \lesssim 4.92$), however, and the system is soon attracted to a new branch of R_1R_2-symmetric periodic orbits created in a saddle-node bifurcation. When, in turn, this R_1R_2-symmetric branch loses stability, we observe a new branch of stable asymmetric periodic orbits created in a nearby saddle-node bifurcation. This sort of alternating transition between R_1R_2-symmetric and asymmetric oscillations is repeated again and again. Note also that the chaotic windows associated with these transitions become narrower and narrower as μ increases. In Fig. 3 we show stable attractors associated with three consecutive periodic windows in Fig. 2. These limit cycles are evidently *relaxation oscillations*, but of an unusual type, involving slow drifts along branches of both equilibria *and* of periodic orbits, with fast jumps between them. Moreover, these oscillations may be symmetric or asymmetric, with the symmetry alternately present and broken in successive periodic windows. In the following we suggest an explanation for this remarkable behavior, cf. [20].

To understand this behavior we rewrite Eqs. (13) in the form

$$\mathbf{X}' \quad \mathbf{F}_1(\mathbf{X},\mathbf{Y},v;\mu), \quad \mathbf{Y}' \quad \mathbf{F}_2(\mathbf{X},\mathbf{Y},v;\mu), \quad v' \quad \varepsilon G(\mathbf{X},\mathbf{Y},v), \tag{15}$$

where $\mathbf{X} = (\mathrm{Re}(X), \mathrm{Im}(X))$, $\mathbf{Y} = (\mathrm{Re}(Y), \mathrm{Im}(Y))$ and suppose that $0 < \varepsilon \ll 1$. The properties of the relaxation oscillations can be understood by examining first the case $\varepsilon = 0$. In this case v becomes a parameter, and Eqs. (15) become

$$\mathbf{X}' = \mathbf{F}_1(\mathbf{X},\mathbf{Y};v,\mu), \quad \mathbf{Y}' = \mathbf{F}_2(\mathbf{X},\mathbf{Y};v,\mu). \tag{16}$$

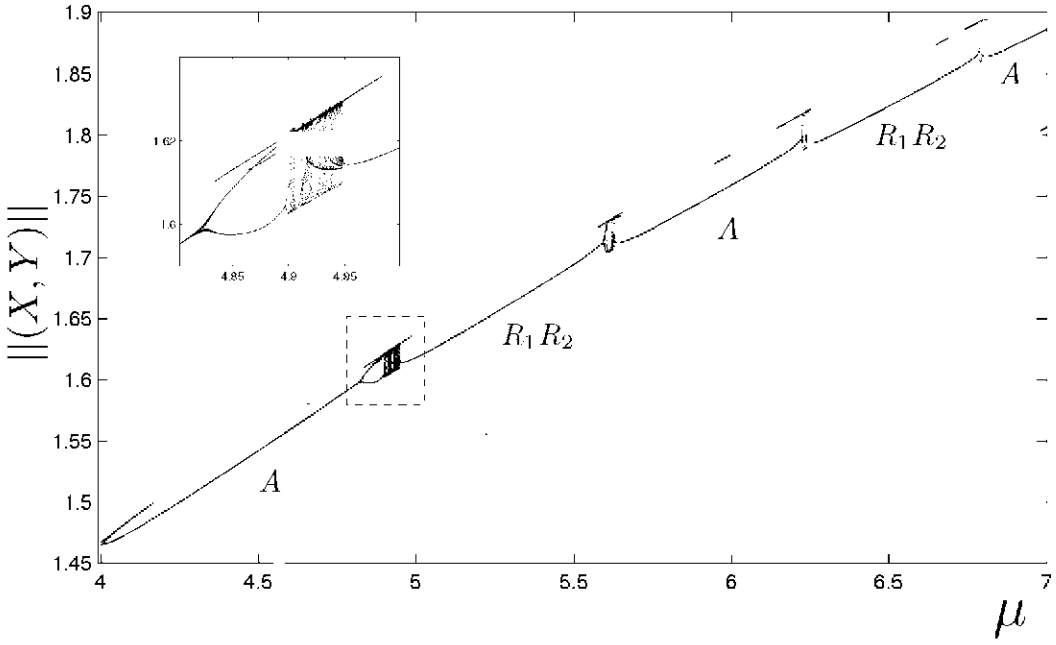

Figure 2. Bifurcation diagram showing an alternating sequence of R_1R_2-symmetric (R_1R_2) and asymmetric (Λ) periodic orbits. The figure is constructed by recording successive maxima of $||(X,Y)|| \equiv \sqrt{||X||^2 + ||Y||^2}$ at each value of μ. The inset shows an enlargement of the first chaotic region.

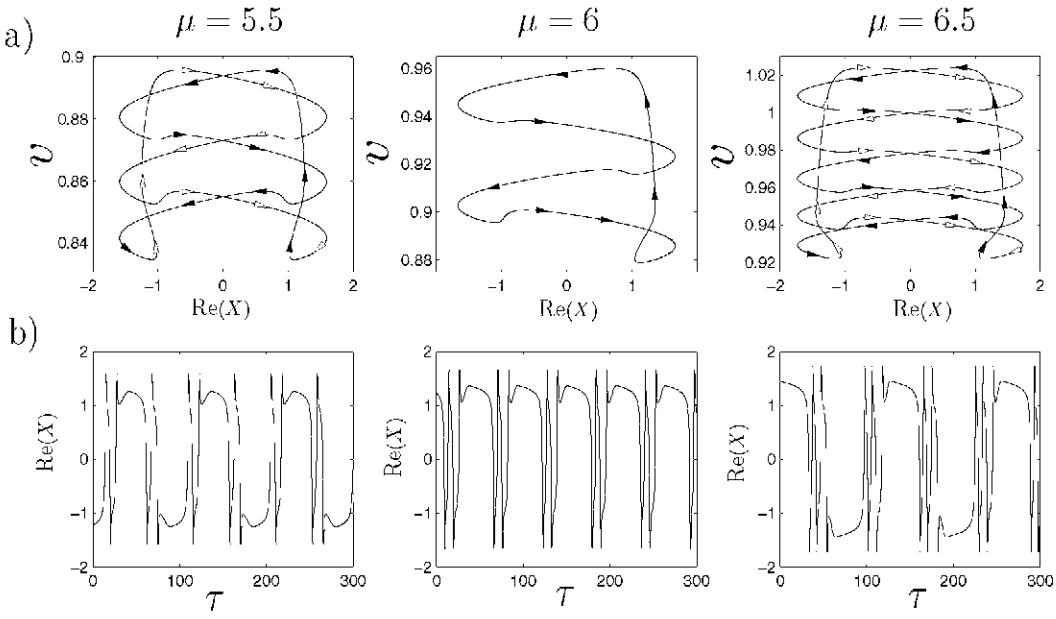

Figure 3. (a) Projection onto the $(\mathrm{Re}(X), v)$ plane of stable symmetric and asymmetric periodic orbits in successive periodic windows in Fig. 2. (b) The corresponding time series $\mathrm{Re}(X(\tau))$.

This pair of equations can have both steady state solutions and periodic solutions. Of particular significance is the one-dimensional nullcline $\Sigma : \mathbf{F}_1(\mathbf{X}, \mathbf{Y}, v; \mu) = \mathbf{F}_2(\mathbf{X}, \mathbf{Y}, v; \mu) = 0$ that contains the steady states when $\varepsilon > 0$ and consists of them when $\varepsilon = 0$. As indicated in Fig. 4 the projection

of Σ onto the $(v, \mathrm{Re}(X))$ plane consists of pairs of branches of stable ($S^{\pm}$) and unstable ($U^{\pm}$) states, related by symmetry. In addition to these branches of steady states Eqs. (16) also contain a one parameter family of attracting *limit cycles*. These periodic solutions are created, as v increases, in a heteroclinic bifurcation involving the two fixed points U^+ and U^-, and are R_1R_2-symmetric. Between this heteroclinic bifurcation and the turning points $q^{\pm}$ the stable R_1R_2-symmetric limit cycles coexist with the stable fixed points $S^{\pm}$ (see Fig. 4). When ε is finite but small these states couple to the slow evolution of the variable v, and the manifolds of steady states and periodic orbits become part of the *slow manifold* of the system (15). In the following we speak of the solutions as drifting along this manifold (the slow phase); this drift proceeds until the system is forced away from the slow manifold, heralding the onset of the fast phase of the oscillation that takes it back to the slow manifold. The plots in Figs. 3 can be interpreted in this light, with episodes of almost constant $\mathrm{Re}(X)$ corresponding to drift along the manifold of steady states $S^{\pm}$ and the return trajectory consisting of a drift along the branch of periodic orbits.

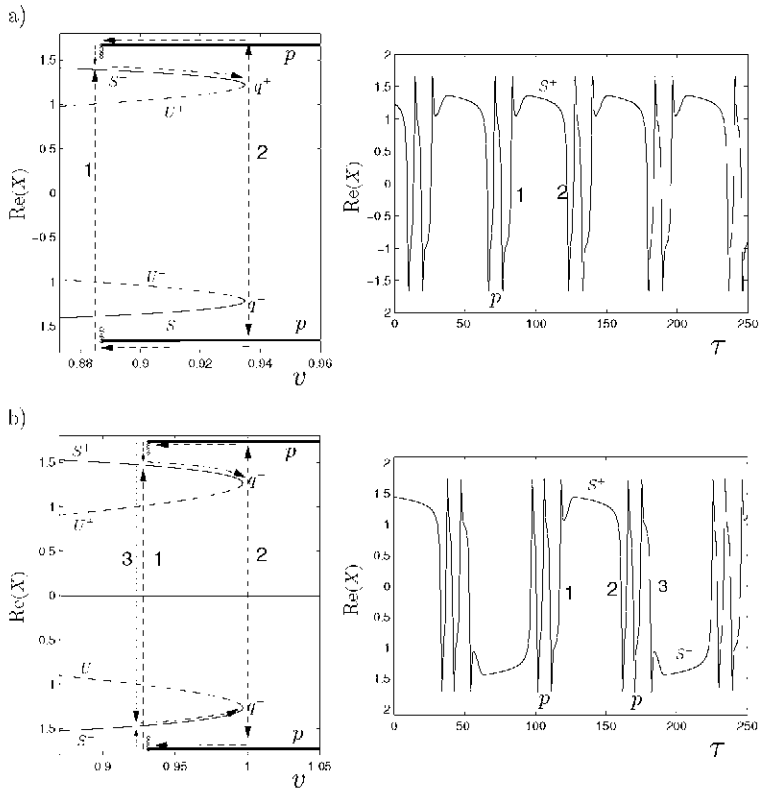

Figure 4. The slow manifold for the system (15) lies within $O(\varepsilon)$ of the manifolds $S^{\pm}$, $U^{\pm}$ of steady states, and the manifold p of periodic orbits, of Eqs. (15) with $\varepsilon = 0$. The slow drifts in v that occur when $0 < \varepsilon \ll 1$ are indicated by broken 'horizontal' arrows; the fast phase results in 'vertical' jumps. These are indicated by vertical arrows, and labeled by integers to indicate the corresponding transition in the associated time series $\mathrm{Re}(X(\tau))$. (a) Asymmetric relaxation oscillations of Eqs. (15) when $\mu = 6.0$ and $\varepsilon = 0.01$. (b) R_1R_2-symmetric relaxation oscillations of Eqs. (15) when $\mu = 6.5$ and $\varepsilon = 0.01$.

To understand the nature of the resulting relaxation oscillations in greater detail we begin by considering the drift along M_S^+, the part of the slow manifold near the stable steady states S^+. The drift is in the direction of increasing v and so takes the system towards q^+ (see Fig. 4). Near this point the slow drift ends and the system jumps abruptly to the branch of symmetric periodic

states, labeled p. In Fig. 4 this transition is indicated by a vertical short-dashed line, and labeled with the number 2. The system then drifts towards the left along the corresponding slow manifold M_p until it reaches the vicinity of the $\varepsilon = 0$ heteroclinic connection where the $\varepsilon = 0$ oscillations disappear, and so does the associated slow manifold M_p ($0 < \varepsilon \ll 1$). With the disappearance of M_p the system is forced to either jump toward S^+ or toward S^-. Which of these two outcomes takes place is determined by the phase of the trajectory near U^+ or U^-. These states are saddles with one unstable direction and three stable directions. In what follows it is important that the least stable eigenvalue is in fact complex. For example, when $\varepsilon = 0$ the eigenvalues of $U^\pm$ at $\mu = 6.5$ are 0.6547, $-0.9999 \pm 14.236i$ and -2.65405, and these values are typical of the other periodic windows as well. The time series show clearly that when the drift along M_p ends the system approaches either $U^|$ or U^- along its stable manifold; what happens thereafter depends on which part of its unstable manifold is followed. If the unstable manifold of $U^|$ (say) takes the system to $S^|$ (as in Fig. 4(a)) the fast phase (labeled 1) terminates on $S^|$ and the system thereafter drifts towards the right along M_S^+. The resulting oscillation is an asymmetric relaxation oscillation. In contrast, if the unstable manifold of $U^|$ takes the system to S^- (cf. Fig. 5) the fast phase terminates on S^- and the system thereafter drifts towards the right along M_S^-. In Fig. 4(b) this transition is labeled 3; the accompanying panel shows the corresponding signature in the time series. When the slow phase terminates the system jumps back to the large amplitude periodic state (transition 2) and drifts along it to the left, but this time when it falls off M_p in the transition labeled 1 it goes to U^- and by symmetry follows *its* unstable manifold towards $S^|$. The resulting trajectory is R_1R_2-symmetric. It is clear that these two outcomes are the result of a π phase change in the direction in which the trajectory enters the neighborhood of $U^|$. Figure 5 shows the oscillations of Fig. 3 in a projection that highlights the role of the stable manifold of these unstable steady states as a separatrix between the two slow phases of the relaxation oscillation.

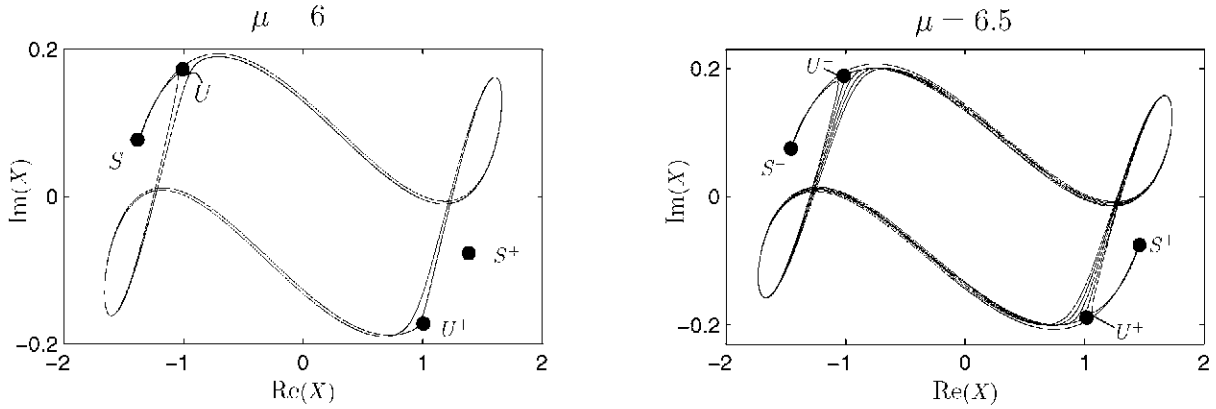

Figure 5. Projections of (a) an asymmetric solution at $\mu = 6.0$ and (b) an R_1R_2-symmetric solution at $\mu = 6.5$ on the $(\mathrm{Re}(X), \mathrm{Im}(X))$ plane, both calculated with $\varepsilon = 0.01$, showing the role played by the stable manifold of $U^\pm$ in determining the part of the slow s table manifold followed by the solution. The actual trajectory spirals around this manifold.

We now turn to the sequence of *transitions* revealed in Fig. 2. The bifurcation diagrams in Fig. 6 show what happens in all transitions from an asymmetric oscillation to a symmetric one, and from a symmetric one to an asymmetric one, as μ increases, while Fig. 7 shows the *period* of the corresponding solutions, also as a function of μ (boxed regions). Each transition is accompanied by a stability gap within which chaotic dynamics (symmetric and asymmetric) are found, and each new periodic solution emerges out of such a region in a saddle-node bifurcation. Figure 7 also shows that in each transition the period of the stable oscillation jumps by an approximately constant

amount, and subsequently decreases along both the stable and the unstable branches away from the saddle-node bifurcation.

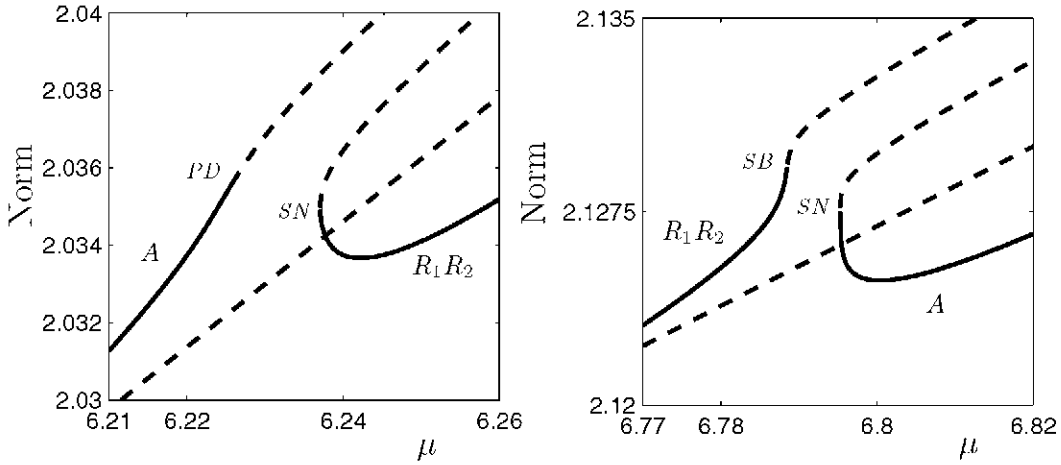

Figure 6. Detail of the bifurcation diagrams near the transition from asymmetric to symmetric relaxation oscillations near (a) $\mu = 6.23$, and (b) $\mu = 6.79$. Solid (broken) lines indicate stable (unstable) solutions. The labels SN, SB and PD denote saddle-node, symmetry-breaking and period-doubling bifurcations, respectively.

Figure 8 focuses on a branch of asymmetric relaxation oscillations that first appears in a saddle-node bifurcation near $\mu = 7.0$, and shows that as one follows the stable branch from the saddle-node towards larger μ one encounters an interval of μ in which the period drops precipitously (Fig. 8(a), inset). Just after this point the stable (asymmetric) relaxation oscillation loses stability via period-doubling (not shown). Figure 8(b) shows the time series at the point marked 3 ($\mu = 7.3118$) just before this loss of stability, and suggests that this loss of stability is a consequence of the fact that the trajectory is beginning to follow the unstable manifold before peeling off towards $S^{\pm}$. By point 5 ($\mu = 7.5533$) the trajectory follows the unstable manifold U^- all the way to the saddle-node at q^-. For yet larger μ the oscillation remains unstable but the trajectory departs from U^- in the *opposite* direction (see point 6, $\mu = 10.0$). These results indicate that with increasing μ the trajectory comes closer and closer to the hyperbolic steady states $U^{\pm}$ resulting in longer and longer drift along the unstable manifold M_U. This fact also suggests an increasing role for the leading eigenvalues of $U^{\pm}$. In the present case the least stable eigenvalue λ_s is complex, but the unstable eigenvalue $\lambda_u < |\mathrm{Re}(\lambda_s)|$. Thus the periodic solutions in the fast system approach the heteroclinic connection *monotonically* and no chaotic dynamics are expected. Section 3 examines the dynamics when this condition does *not* hold.

Stable bursting behavior of the type shown in Figs. 3, 4 and 8 becomes increasingly dramatic as μ is increased, revealing ever more clearly the two slow phases and the rapid transition between them. In Fig. 9(a) we show a stable oscillation for $\varepsilon = 0.01$ and $\mu = 9.0$ projected onto the $(||(X,Y)|| \equiv \sqrt{||X||^2 + ||Y||^2}, v)$ plane, cf. Fig. 4, and superposed on the slow manifold computed with $\varepsilon = 0$. We see that during one part of the slow phase (labeled 1) the system drifts towards smaller v along the slow manifold M_p of stable periodic solutions p. Near the heteroclinic connection in the fast system the oscillations end and the system undergoes a rapid transition to the stable manifold M_S indicated by a vertical arrow. Thereafter it enters a new slow phase, labeled 2, and drifts in the direction of increasing v, towards the fold point q, where the slow phase ends and the system makes a rapid transition back to M_p. This transition is also indicated by a vertical arrow. The small cusp-like feature at the onset of phase 2 results from a brief visit of the trajectory near

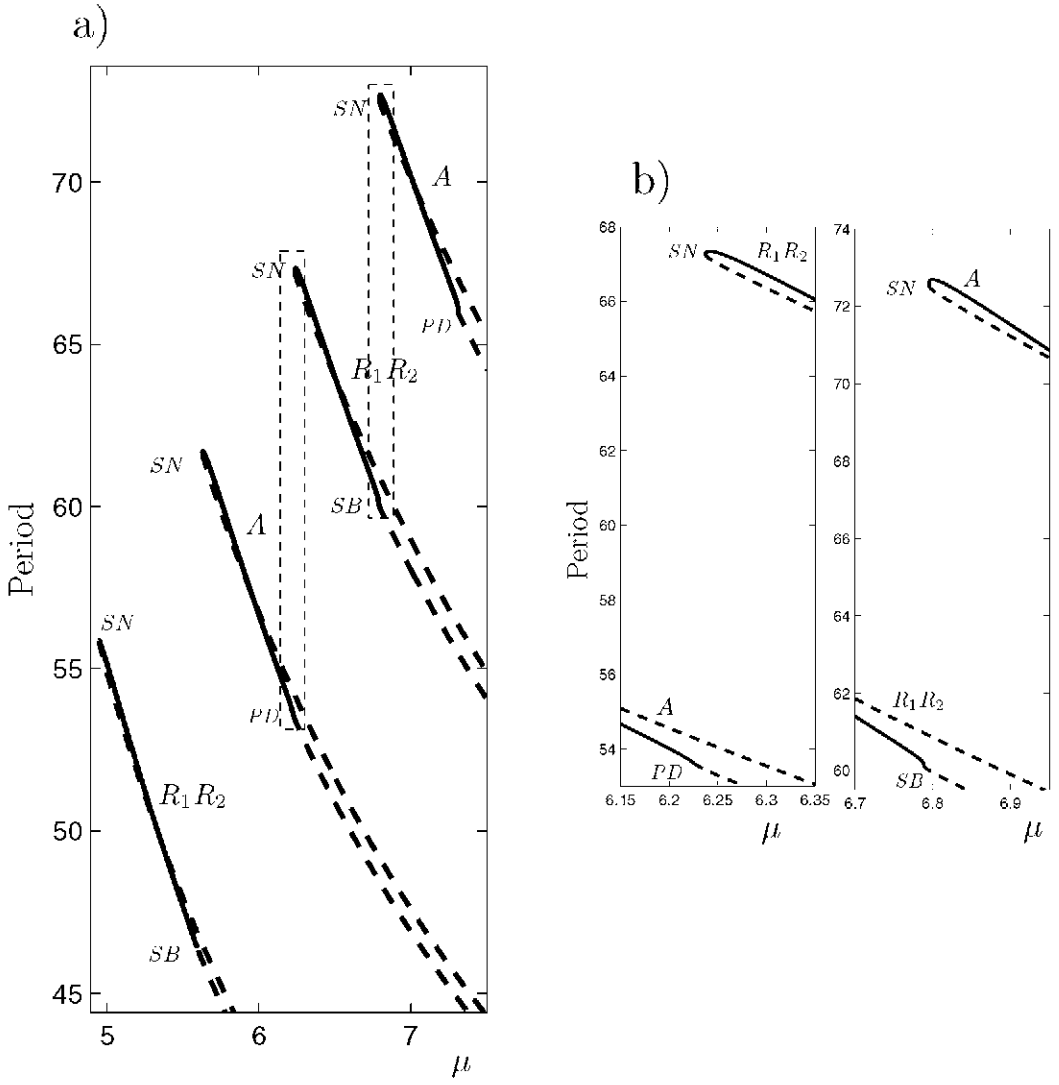

Figure 7. Alternating sequence of R_1R_2-symmetric and asymmetric relaxation oscillations. The diagram show the period (half-period) of asymmetric (symmetric) periodic relaxation oscillations as a function of μ. Solid (dashed) line corresponds to stable (unstable) states. The labels SN, SB and PD denote saddle-node, symmetry-breaking and period-doubling bifurcations, respectively.

the unstable slow manifold M_U, before being ejected towards the stable slow manifold M_S. As μ increases and the next symmetry-switching transition is approached the solutions spend more and more time near M_U, and hence involve longer and longer episodes of drift along M_U. Figures 9(b,c) show two examples of this behavior, differing only slightly in the value of μ. In the first of these the system drops to the unstable steady state at the end of the slow phase 1, and then drifts along M_U towards larger v before a sudden jump to M_S. The slow drift continues along M_S towards the fold on Σ where the system jumps to the oscillatory state p, and the slow phase 1 recommences. In contrast the solution in Fig. 9(c) jumps from M_U to M_p (instead of M_S) and so begins to drift towards smaller v but the next time, instead of following M_U, it jumps to M_S and begins to follow the standard relaxation oscillation scenario. Even more exotic possibilities are displayed in Fig. 10. The remarkable sensitivity to the value of μ is evidently a consequence of the amplification of small differences in the approach of the trajectory towards M_U by the unstable eigenvalue of U, and heralds

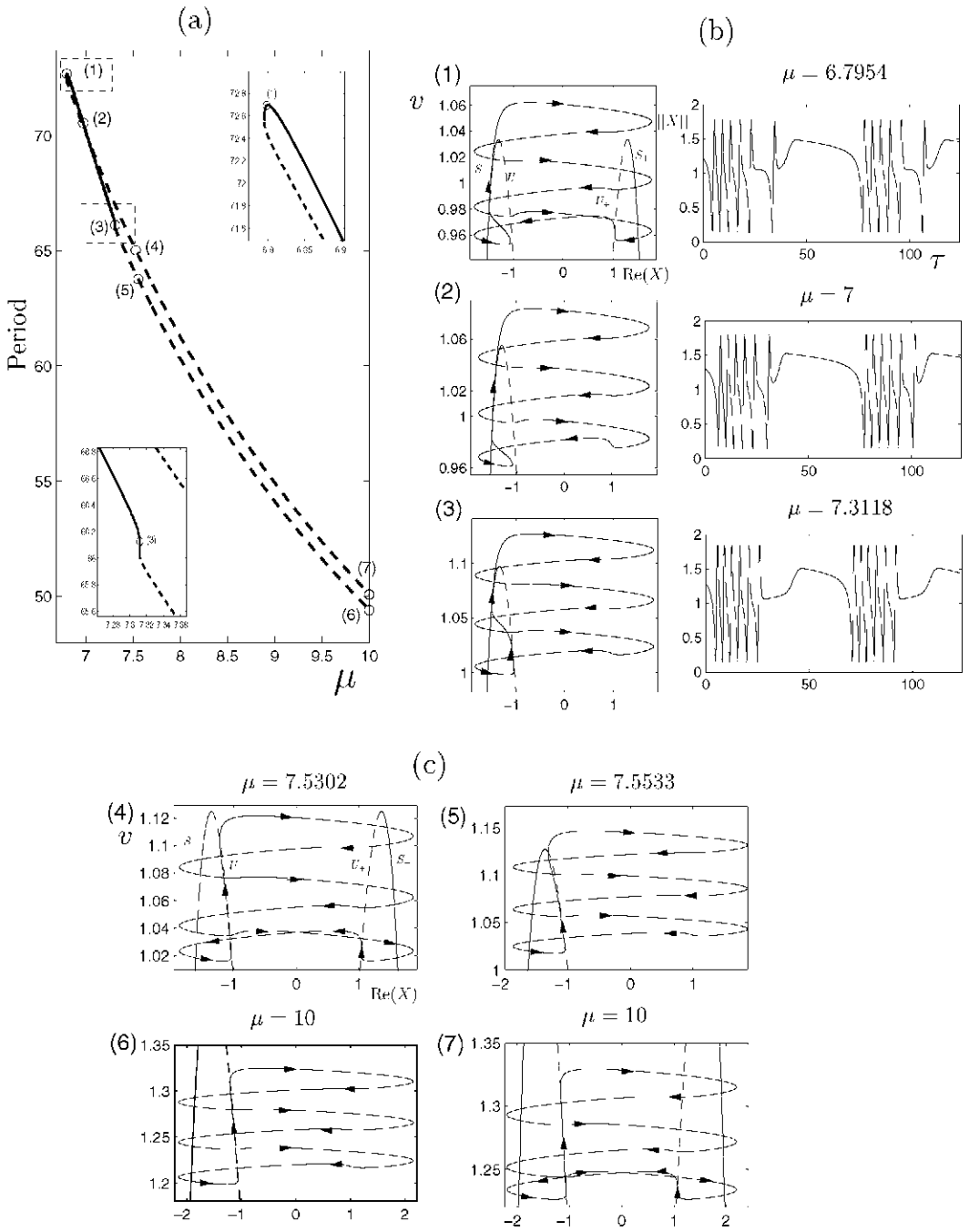

Figure 8. (a) Period of asymmetric relaxation oscillations as a function of μ. Solid (dashed) lines correspond to stable (unstable) states. (b) Stable relaxation oscillations corresponding to the open circles (1,2,3) in figure (a) projected on the $(\mathrm{Re}(X), v)$ plane together with the corresponding time series $||X(\tau)||$. (c) Unstable relaxation oscillations corresponding to the remaining open circles (4,5,6) in figure (a) in the same projection.

the transition from asymmetric oscillations to symmetric ones: in effect, with each half-turn around $U^{\pm}$ the trajectory changes the direction in which it leaves $U^{\pm}$, and hence its symmetry. In addition its period jumps by a finite amount, a phenomenon we have already noted. When the number

of turns increases monotonically with μ there will be an infinite sequence of symmetry-changing transitions, and hence a sequence of periodic windows with alternating symmetric and asymmetric relaxation oscillations. Thus each saddle-node bifurcation creates a pair of periodic orbits with an extra half-turn. Moreover, since it takes a finite interval in μ to change the frequency sufficiently to add a half-turn these symmetry-changing transitions cannot accumulate, in contrast to the cascades of symmetry-switching gluing bifurcations that occur in other D_2-symmetric systems [7]. For other parameter choices (e.g., $\Gamma = 0.7$, $\Lambda = -0.6$, $0.35 \leq \gamma < 0.4$, not shown) the number of transitions is finite.

3. Square domains

Simonelli and Gollub ([19]) performed detailed experiments in square and almost square containers, focusing on the interaction of modes $(3,2)$ and $(2,3)$. In a square container these modes are related via a reflection in the diagonal and hence bifurcate simultaneously from the flat state. Abstract theory also shows that a mixed mode state, consisting of an equal amplitude superposition of these two states, bifurcates at the same point. Both these states are periodic in time, and in the square container Simonelli and Gollub found no other states near the primary bifurcation. The situation becomes quite different in a rectangular container. In a container of horizontal aspect ratio 1.07 Simonelli and Gollub found dramatic relaxation oscillations near the mode interaction point, and these could be periodic or chaotic. These oscillations consisted of a long period oscillation (up to 2 hr) in the amplitudes of the $(3,2)$ and $(2,3)$ modes, a period much longer than the period of the modes themselves (0.07s). To the authors' knowledge no detailed explanation for this remarkable behavior has been provided, although several suggestions have been made [16]. Given the resemblance of this behavior to that described in Sect. 2.3 for the elliptically distorted cylinder, we explore here the possibility that the observed relaxation oscillations are a consequence of the coupling of the two modes with a streaming flow.

In the case of an almost square rectangular domain the coupled amplitude-streaming flow equations take the form [8]

$$\begin{aligned} A'_{\pm}(\tau) = &- [1 + i(\Gamma \pm \Lambda)]A_{\pm} + i\mu A_{\pm} + i(\alpha_1|A_{\pm}|^2 + \alpha_2|A_{\mp}|^2)A_{\pm} + i\alpha_3 A_{\mp}^2 A_{\pm} \\ &\pm \Omega \int_{-1}^{0} \int_{\Sigma} \mathbf{u} \cdot \mathbf{g} d\mathbf{x} A_{\mp}, \\ \partial \mathbf{u}/\partial \tau &- [\mathbf{u} + \mathbf{G}(A_+, A_-)] \times (\nabla \times \mathbf{u}) = -\nabla p + Re^{-1} \Delta \mathbf{u}, \end{aligned}$$

with appropriate boundary conditions on $\mathbf{u}$. Here $A_{\pm}$ are amplitudes of two eigenfunctions that are related by reflection in the xy diagonal of the square, e.g., the $(3,2)$ and $(2,3)$ spatial modes of the system,

$$\mathbf{G} \equiv i(A_+ \bar{A}_- - \bar{A}_+ A_-)(\mathbf{g} - \mathbf{h}),$$

where $\mathbf{g}$ and $\mathbf{h}$ are known functions, and the remaining quantities have their earlier meaning.

When $\Lambda = 0$ these equations are symmetric with respect to the two reflections

$$x \to -x, \quad A_| \to -A_|, \quad (u_1, u_2, u_3) \to (-u_1, u_2, u_3) \tag{17}$$

and

$$x \to y, \quad A_+ \to A_-, \quad (u_1, u_2, u_3) \to (u_2, u_1, u_3) \tag{18}$$

that generate the group of symmetries of a square. When $\Lambda \neq 0$ (18) is no longer a symmetry, and the equations are invariant under (17) and

$$y \to -y, \quad A_- \to -A_-, \quad (u_1, u_2, u_3) \to (u_1, -u_2, u_3)$$

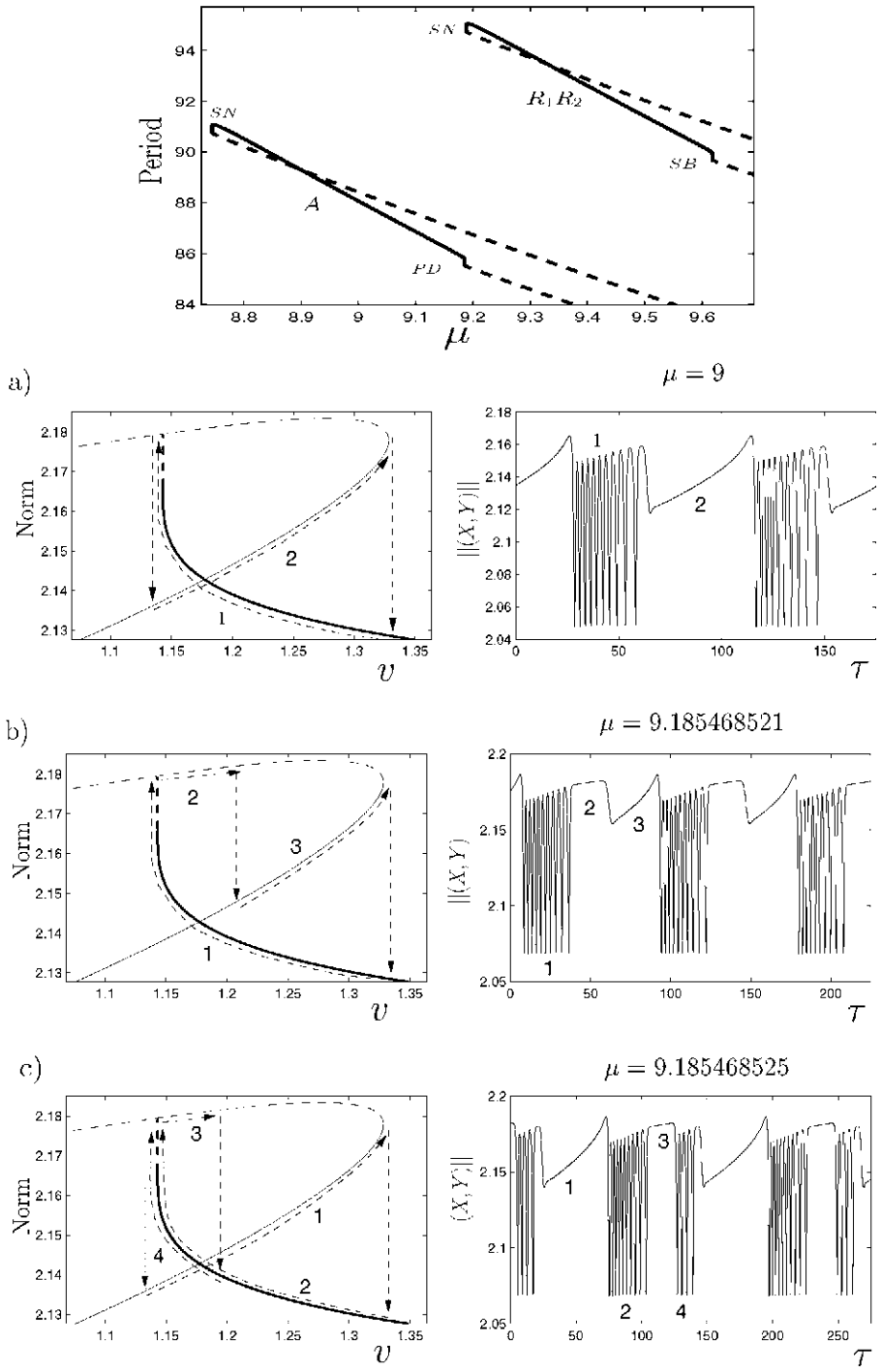

Figure 9. Stable asymmetric relaxation oscillations for (a) μ 9, (b) μ 9.185468521 and (c) μ 9.185468525. The top panel shows the location of these solutions in a period vs μ plot (Fig. 7). The slow drifts, present when $0 < \varepsilon \ll 1$, are labeled with numbers to indicate the corresponding phase in the accompanying time series $||(X, Y)||$, computed from Eqs. (15) with ε 0.01. The arrows indicate the direction of drift as well as the fast transitions.

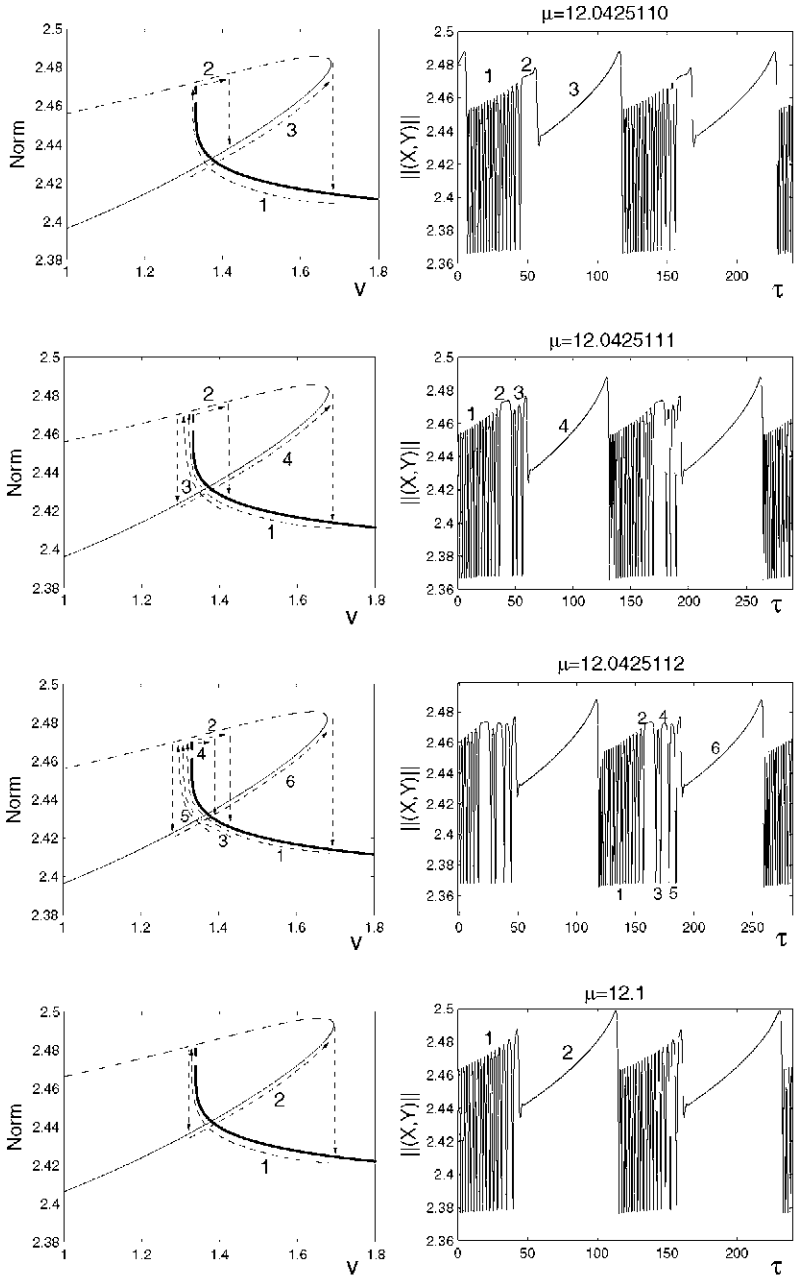

Figure 10. More exotic relaxation oscillations near $\mu = 12$.

only. We can now proceed as in the case of the cylindrical container, and project onto the slowest mode of the square. In general, however, the mean flow will contain contributions that are odd/odd, odd/even, even/odd and even/even with respect to the symmetries (17), (18), of which only the first couples to the amplitude equations. The simplest model problem that captures the coupling between the amplitudes and the streaming flow is therefore given by [8]

$$\begin{aligned} X' &= -(1+i(\Gamma+\Lambda))X + i(\alpha_1|X|^2+\alpha_2|Y|^2)X + i\alpha_3\overline{X}Y^2 + i\mu\overline{X} - \gamma vY, \\ Y' &= -(1+i(\Gamma-\Lambda))Y + i(\alpha_1|Y|^2+\alpha_2|X|^2)Y + i\alpha_3\overline{Y}X^2 + i\mu\overline{Y} + \gamma vX, \\ v' &= \varepsilon(-v + i(\overline{X}Y - X\overline{Y})), \end{aligned} \tag{19}$$

where $X = A_{|}$, $Y = A_{-}$ and v represents the odd/odd part of the streaming flow. The use of the variables X and Y emphasizes the similarity between this system and (13). In particular Eqs. (19) are equivariant with respect to the group D_2 generated by the two reflections (14). As a result there are again two types of steady states, pure modes and mixed modes. The former are given by $P_{|} \equiv (0, Y, 0) = (0, R_{|}\, e^{i\phi_+}, 0)$ and $P_{-} \equiv (X, 0, 0) = (R_{-} e^{i\phi_-}, 0, 0)$, with $P_{|}$ invariant under R_1 and P_{-} invariant under R_2. This time, however, there are two types of mixed modes, *in-phase mixed modes* [4] given by $Ms \equiv (X, Y, 0) = (R_{-} e^{i\phi_-}, R_{|}\, e^{i\phi_+}, 0)$ with $\phi_{-} = \phi_{|}$, and *general mixed modes* given by $MM \equiv (X, Y, v) = (R_{-} e^{i\phi_-}, R_{|}\, e^{i\phi_+}, v)$, $XYv \neq 0$. Neither of these has a reflection symmetry.

3.1. Results

For distilled water in a square container of depth $d = 2.5$cm and horizontal cross-section 6.17×6.17cm vibrated vertically with frequency close to twice the natural frequency associated with the inviscid mode $(m, n) = (3, 2)$ inviscid theory gives $\alpha_1 = -0.194057$, $\alpha_2 = 0.026513$, $\alpha_3 = -0.274717$ [1, 4]. The change of the horizontal cross-section to $6.17\text{cm} \times 6.6\text{cm}$ introduces a nonzero value Λ into the equations; we assume, however, that this change in aspect ratio is small enough that the nonlinear coefficients α_1, α_2, α_3 remain unaffected. Finally, we use viscous linear theory to estimate the decay rate of the $(3, 2)$ mode and of the associated streaming flow. We obtain $\delta = 0.001$, $\tilde{\delta} = 0.0001$, respectively, and scale the equations with respect to the former. Thus $\varepsilon = 0.1$ and $\Lambda = 1.6$. As in the elliptical case the coefficient γ remains unknown, and we explore two cases that appear to be relevant to the experiments.

Theories that respect the D_4 symmetry of the square container (e.g., [18]) show that when $\Lambda = 0$ the modes P and Ms bifurcate simultaneously from the flat state. In addition the theory reveals the presence of secondary branches of MM that allow the transfer of stability between the P and Ms states. When the P and Ms branches bifurcate in opposite directions these secondary states can undergo a Hopf bifurcation, but no Hopf bifurcations are otherwise present. When $\Lambda \neq 0$ the breaking of the square symmetry splits the primary bifurcation into two successive bifurcations to pure modes; the loss of reflection symmetry in the diagonal also implies that Ms no longer bifurcate from the flat state, and bifurcate instead from the pure modes in secondary bifurcations. These secondary bifurcations should not be confused with the secondary branches to MM when persist when Λ / 0. However, the coupling to the mean flow introduces a new class of oscillatory instabilities as well [8]. These have a dramatic effect on the bifurcation diagrams because they can occur on the *primary* pure mode branches. Such bifurcations produce an oscillating contribution involving the competing pure mode, together with an oscillating mean flow contribution, and appear via Takens-Bogdanov bifurcations on the $P_{\pm}$ branches. Figure 11 shows typical bifurcation sets for these branches in the two cases (a) γ -0.2 and (b) γ -0.01, i.e., the amplitude on the $P_{\pm}$ branches at which various secondary bifurcations occur, as a function of the detuning Γ.

Figure 12 shows the associated bifurcation diagrams in case (a) for four different values of the detuning Γ. Since $\Lambda > 0$ the mode P_{-} bifurcates before P_{+} when $\Gamma < 0$ and conversely when $\Gamma > 0$. In Fig. 12(a) both branches bifurcate subcritically, and so are initially unstable. However, P_{-} acquires stability at a saddle-node bifurcation SN_{-} but loses it again at a symmetry-breaking bifurcation that produces the secondary states MM (Fig. 13(a)). No steady states are stable beyond this point. Since this point lies to the left of the primary instability to P_{-} the primary instability *must* produce time-dependence. In Fig. 12(b) the detuning is smaller, and P_{-} bifurcates supercritically, before losing stability to MM much as in (a); cf. Fig. 13(b). In Fig. 12(c) $\Gamma > 0$ and the first instability is to P_{+}. The bifurcation to P_{+} is subcritical but the P_{+} branch remains unstable even above the secondary saddle-node bifurcation SN_{+}. This is a consequence of an unexpected Hopf bifurcation on the P_{+} branch below the saddle-node bifurcation. In this case there are therefore no stable steady states near either of the primary instabilities, although P_{-} does become stable briefly at larger amplitude, after shedding an Ms branch (Fig. 13(c)). Finally, in case (d) the pure modes

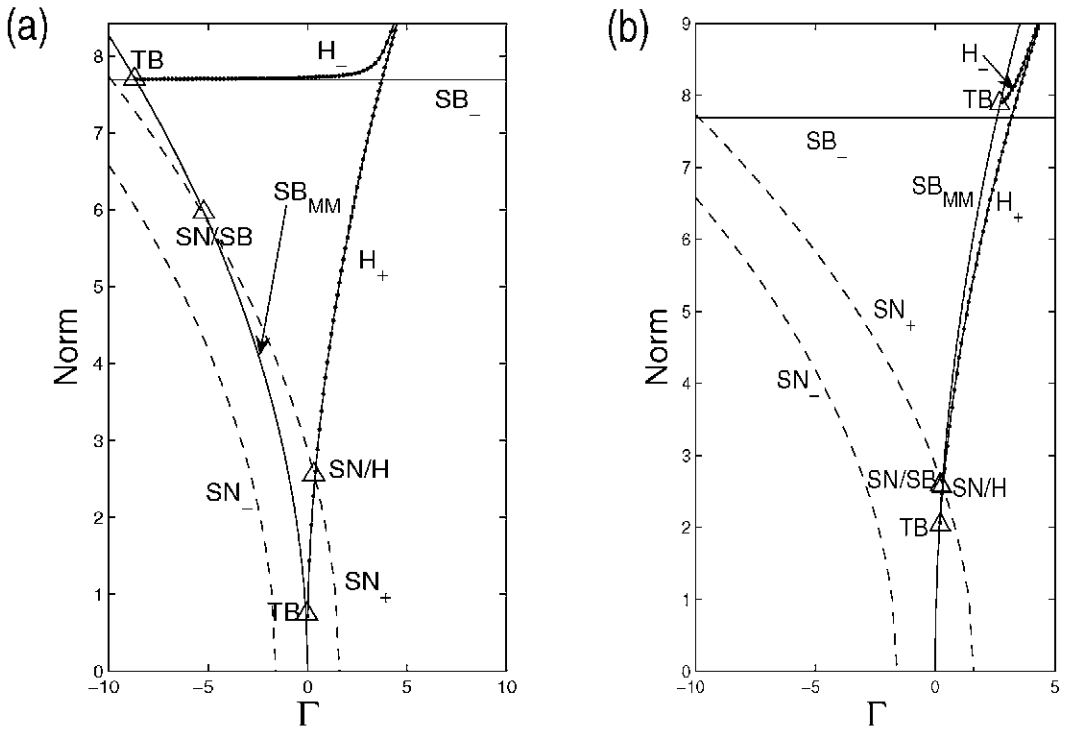

Figure 11. Bifurcation sets of the pure modes $P_{\pm}$ as a function of the Euclidean norm $||(X,Y|| \equiv \sqrt{|X|^2+|Y|^2}$ and the parameter Γ for (a) $\gamma \quad -0.2$, and (b) $\gamma \quad -0.01$. Saddle-node, symmetry-breaking and Hopf bifurcations are labeled by $SN_{\pm}$, $SB_{-,MM}$ and $H_{\pm}$, respectively. The triangles indicate codimension-two points. Takens-Bogdanov, saddle-node/Hopf and saddle-node/symmetry-breaking bifurcations are labeled by TB, SN/H and SN/SB, respectively.

P_+ bifurcate supercritically and remain stable until a secondary Hopf bifurcation H_+. This stability interval overlaps with the stability interval of P_-, between SB_- and H_-, also present in case (c). The bifurcation diagrams in Fig. 12 demonstrate dramatically the role played by the streaming flow: without this flow there would be *no* Hopf bifurcations on the primary branches $P_{\pm}$, and the behavior of the system would be quite different. Figure 13(b) shows the only example of a Hopf bifurcation that persists in absence of the streaming flow (cf., [10]).

Figure 14 shows the corresponding results for $\gamma = -0.01$. Here $P_|$ bifurcates first but does so subcritically. Moreover, this branch undergoes two further bifurcations, a Hopf bifurcation and a symmetry-breaking bifurcation to MM, prior to a saddle-node bifurcation. As a result the $P_|$ branch is once unstable above $SN_|$ while the MM branch is initially twice unstable. Since the MM branch ends in a *supercritical* bifurcation on P_- it must therefore change its stability between $P_|$ and P_-. The simplest way of doing this, confirmed numerically, is via a single tertiary Hopf bifurcation, labeled II in Fig. 14(b). As a result the only stable steady state found near the primary bifurcation is the MM state, beyond II. In the example shown II is to the left of the primary bifurcation, although for other parameter values this point can fall to the right; in the latter case the primary instability leads directly into time-dependent behavior. A similar scenario is also present in an elliptical domain, where it produces the remarkably rich dynamics described in [6].

In Fig. 15 we show some of the dynamical behavior created in the bifurcation II_- on P_- in Fig. 12(d). This bifurcation is found to be *subcritical*; the resulting periodic orbit acquires stability at a saddle-node bifurcation, before undergoing a symmetry-breaking bifurcation, followed by a

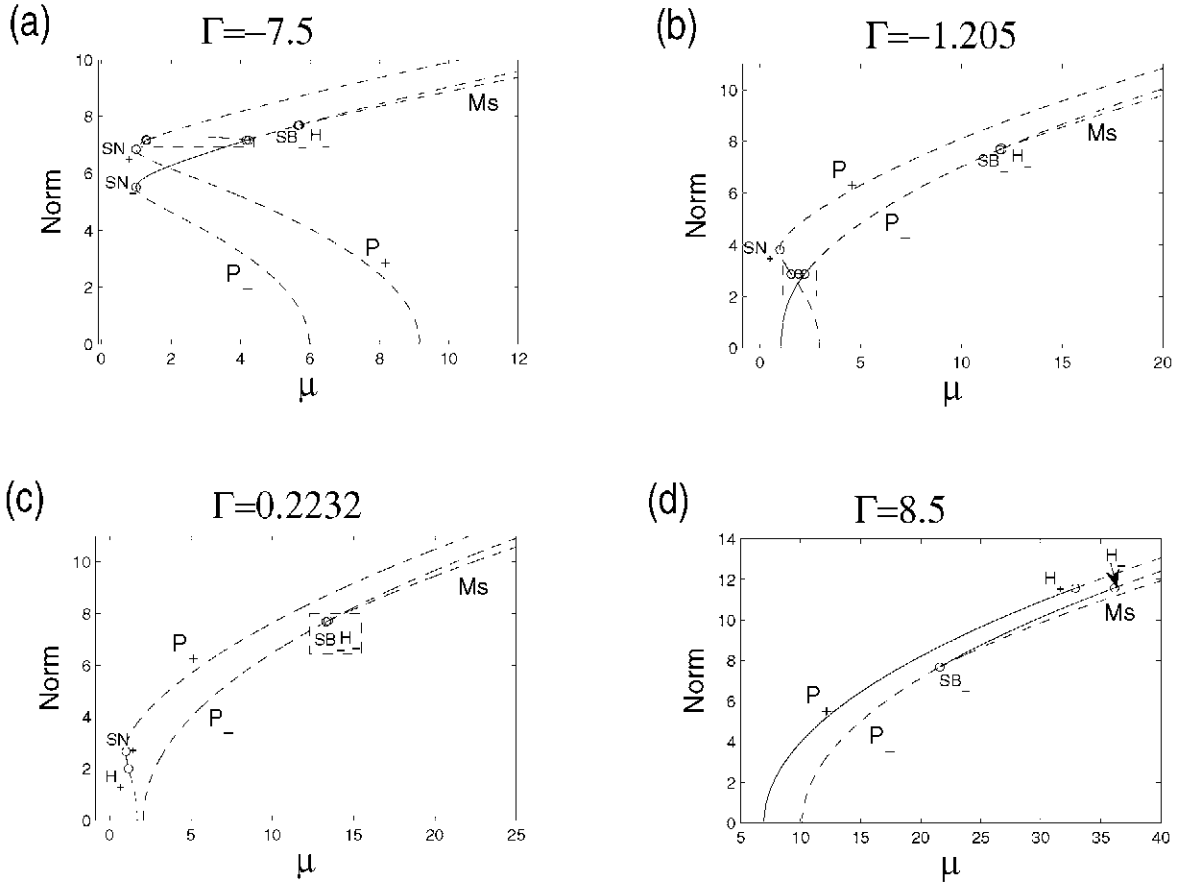

Figure 12. Bifurcation diagrams for the pure modes $P_{\pm}$, and the mixed modes Ms and MM, showing the Euclidean norm $||(X, Y, v)|| \equiv \sqrt{|X|^2 + |Y|^2 + v^2}$ as a function of μ for (a) Γ -7.5, (b) Γ -1.205, (c) Γ 0.2232 and (d) Γ 8.5, when γ -0.2 (Fig. 11(a)). Solid (dashed) lines correspond to stable (unstable) steady states.

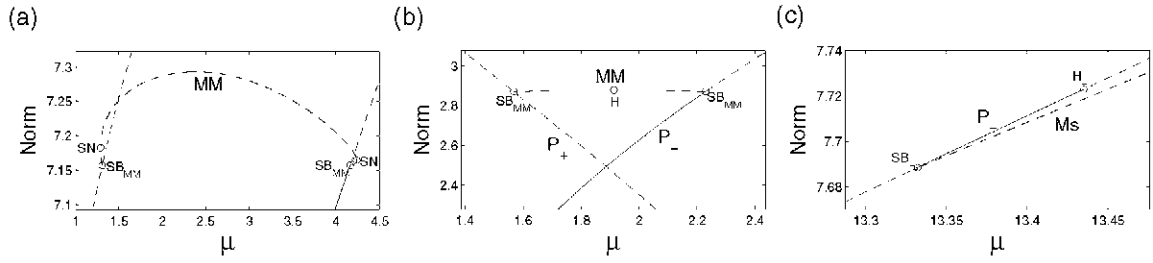

Figure 13. Enlargement of the framed regions in Fig. 12.

cascade of period-doubling bifurcations, the first of which is shown in Fig. 15(c) projected onto the (Re(X),Re(Y)) plane. This projection corresponds to that used by Simonelli and Gollub ([19]) in their figure 13, and allows us to conclude that most likely the behavior in this figure is produced by a scenario similar to Fig. 15. Figure 16 shows the corresponding time series.

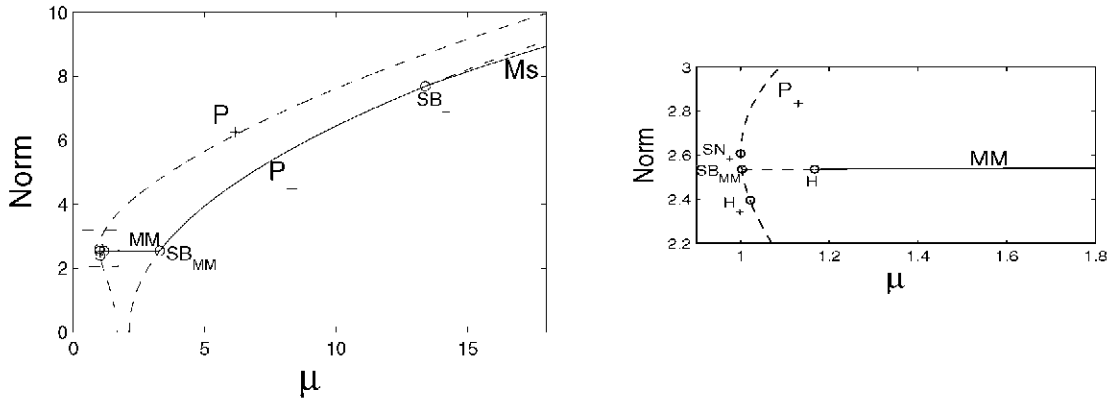

Figure 14. (a) Bifurcation diagram for the pure modes $P_{\pm}$, and the mixed modes Ms and MM, showing the Euclidean norm $||(X,Y,v)|| \equiv \sqrt{|X|^2 + |Y|^2 + v^2}$ as a function of μ for $\Gamma = 0.28$, $\gamma = -0.01$. Solid (dashed) lines correspond to stable (unstable) steady states. (b) Enlargement of the framed region in (a).

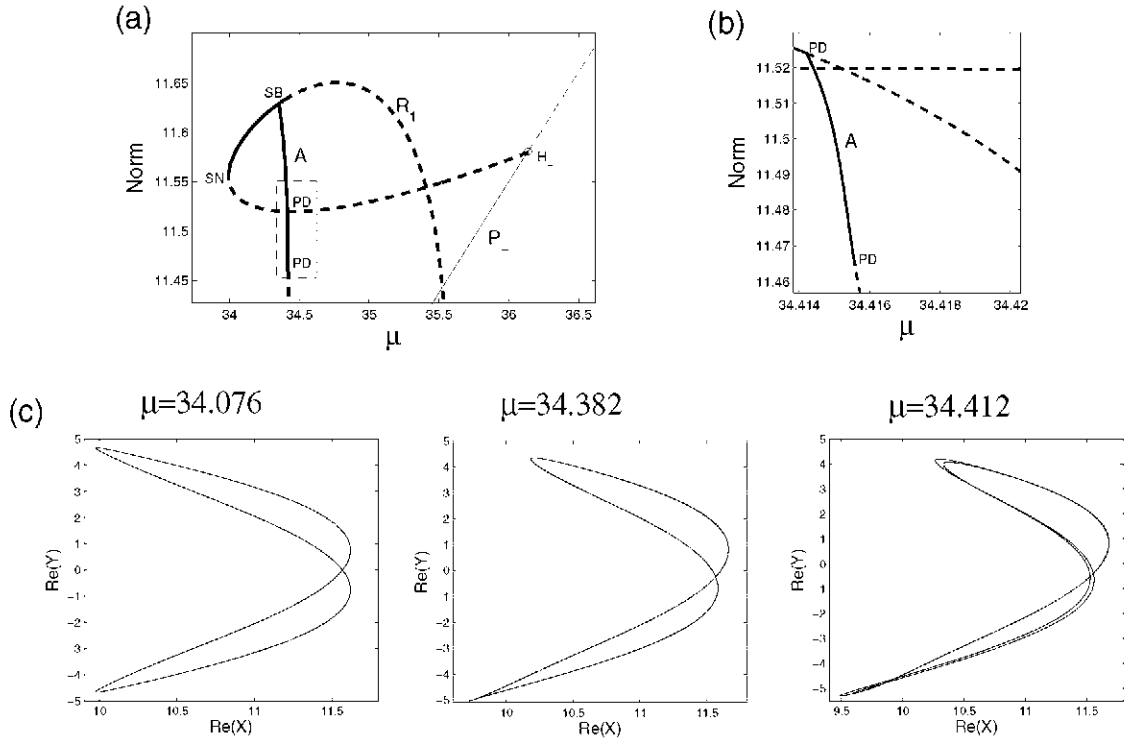

Figure 15. (a) Branches of steady states and periodic orbits in terms of the Euclidean norm $||(X,Y,v)||$ and the L_2 norm $||(X,Y,v)||_{L_2}$, respectively, as a function of μ in case (d) of Fig. 12. Thick solid (dashed) lines indicate stable (unstable) periodic orbits produced in a subcritical Hopf bifurcation H_- on P_-, while thin solid (dashed) lines indicate stable (unstable) steady states. (b) Enlargement of the framed region in (a). (c) Periodic orbits on stable branches in (a), at the indicated values of μ.

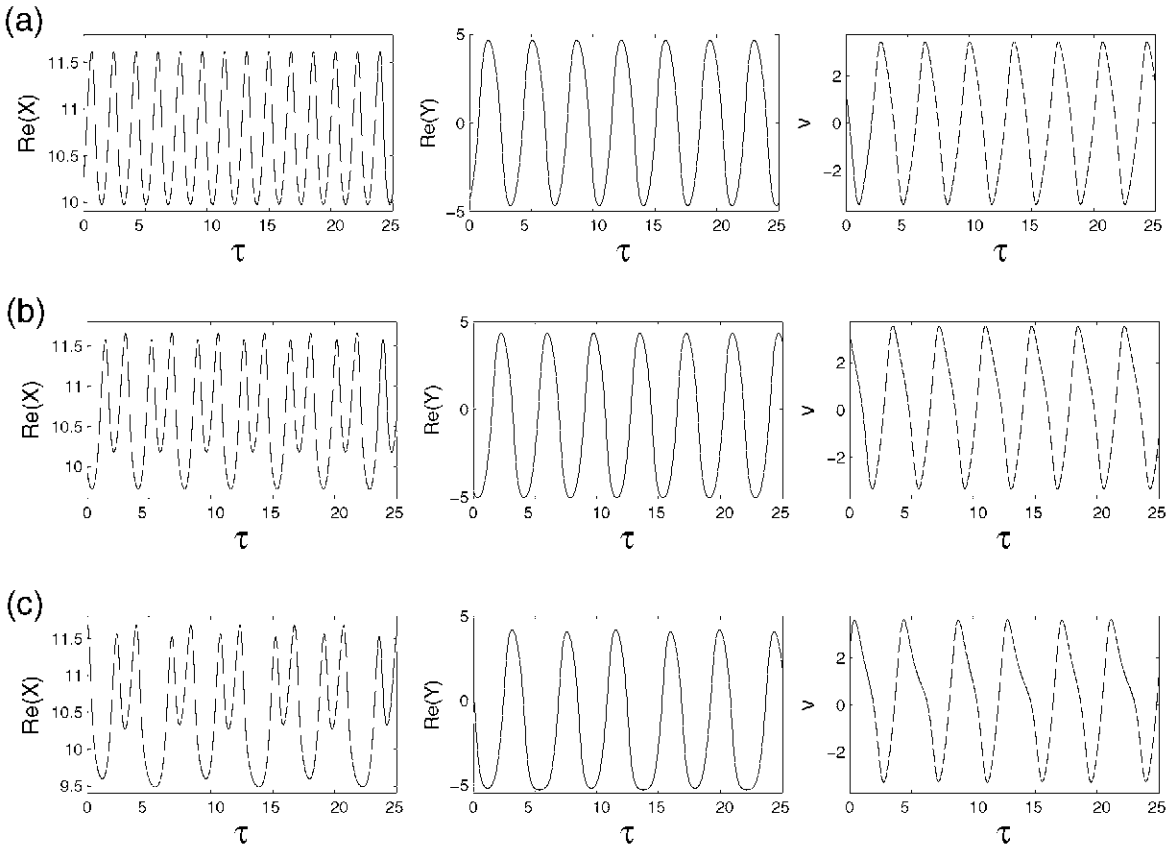

Figure 16. Time series corresponding to the attractors in Fig. 15(c).

3.2. Chaotic dynamics near onset

Chaotic dynamics near onset are found for positive detuning in the range $\Gamma_{TB} \lesssim \Gamma \lesssim \Gamma_{SN/H}$ (Fig. 11(a)). Figure 17 shows three examples, projected onto the (Re(X),Re(Y)) plane, while Fig. 18 shows the corresponding time series. Together these figures suggest the presence of *two* gluing bifurcations. Specifically, in Figs. 17(a) and 18(a) we see that Re(X) and Re(Y) not only both oscillate about zero, but that both approach the origin essentially simultaneously. Since the forcing of the streaming flow vanishes when Re(X) = Re(Y) = 0 the streaming flow decays exponentially during this phase, but jumps to a larger value as soon as Re(X) and Re(Y) become nonzero again. In Figs. 17(b) and 18(b) Re(X) still oscillates about zero but Re(Y) remains positive. Symmetry with respect to R_2 indicates that a reflected solution must also exist, suggesting that the symmetric attractor in Fig. 17(a) is produced by the gluing of these two asymmetric attractors in a *symmetry-increasing* bifurcation, even though the parameter values shown are still far from the required global bifurcation. This conjecture is supported by Fig. 18(b) which shows that both Re(X) and Re(Y) are close to the origin at the same time. Indeed, while Re(X) drifts towards the origin, Re(Y) drifts slowly away from it, eventually triggering a large excursion in Re(Y) before an abrupt return to the origin. The streaming flow once again decays freely when both Re(X) and Re(Y) are small but picks up dramatically during each excursion from the origin. It is this increase in v that arrests the growth of Re(Y) and initiates the return to the origin. Finally, in Fig. 18(c) the time series in Re(X) is more symmetric, and the system approaches the origin during both upward *and* downward swings. These occur more frequently as might be expected of a larger detuning.

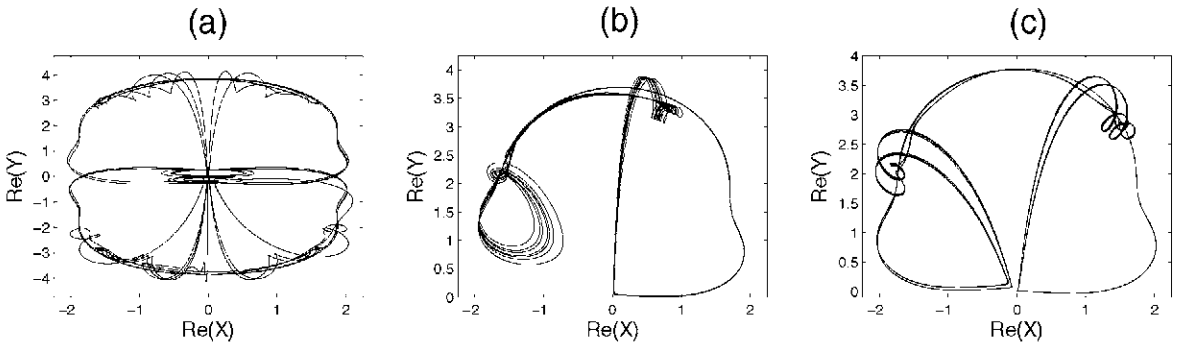

Figure 17. Asymmetric chaotic attractors for the parameters corresponding to Fig. 11(a) between the two codimension-two points TB and SN/H. (a) $\Gamma = 0.2232$, $\mu = 1.75$, (b) $\Gamma = 0.3125$, $\mu = 1.66$, and (c) $\Gamma = 0.33$, $\mu = 1.74$.

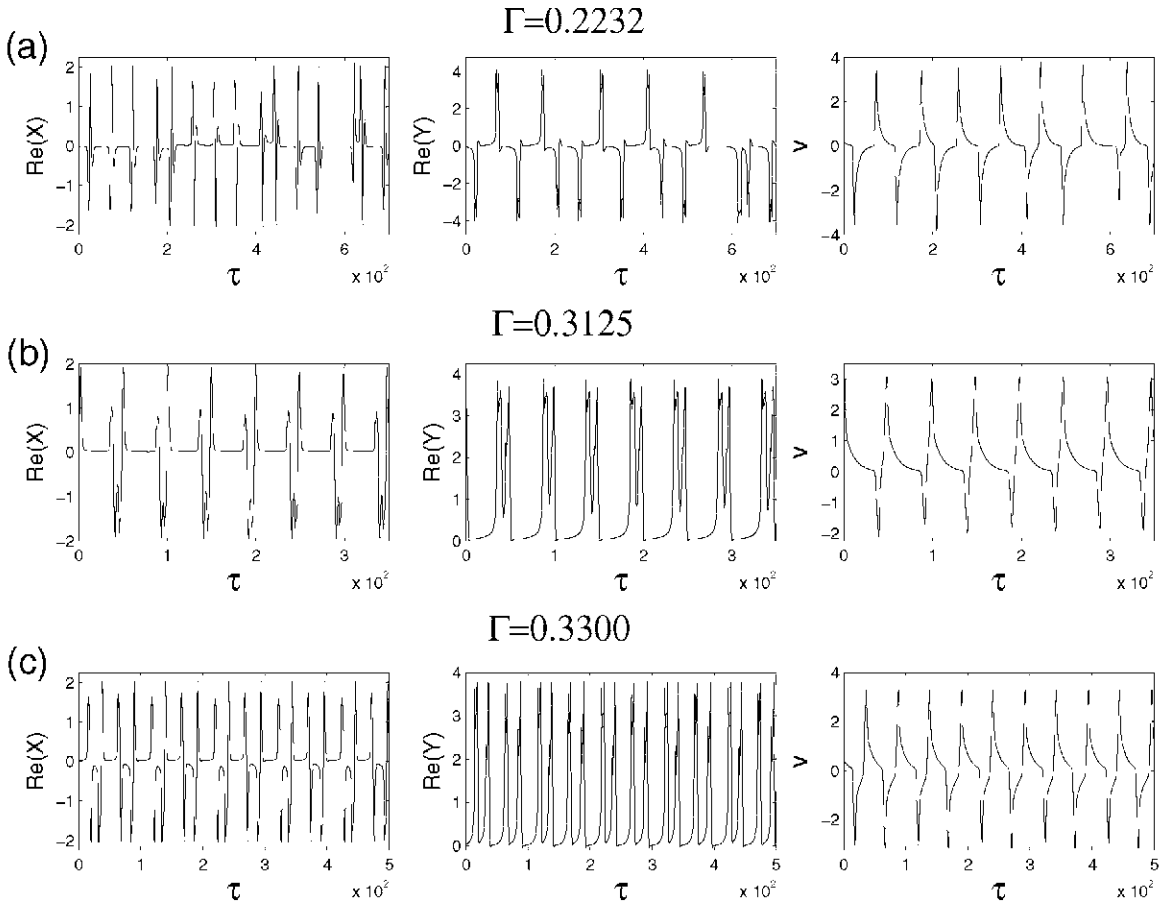

Figure 18. Time series corresponding to the attractors in Fig. 17.

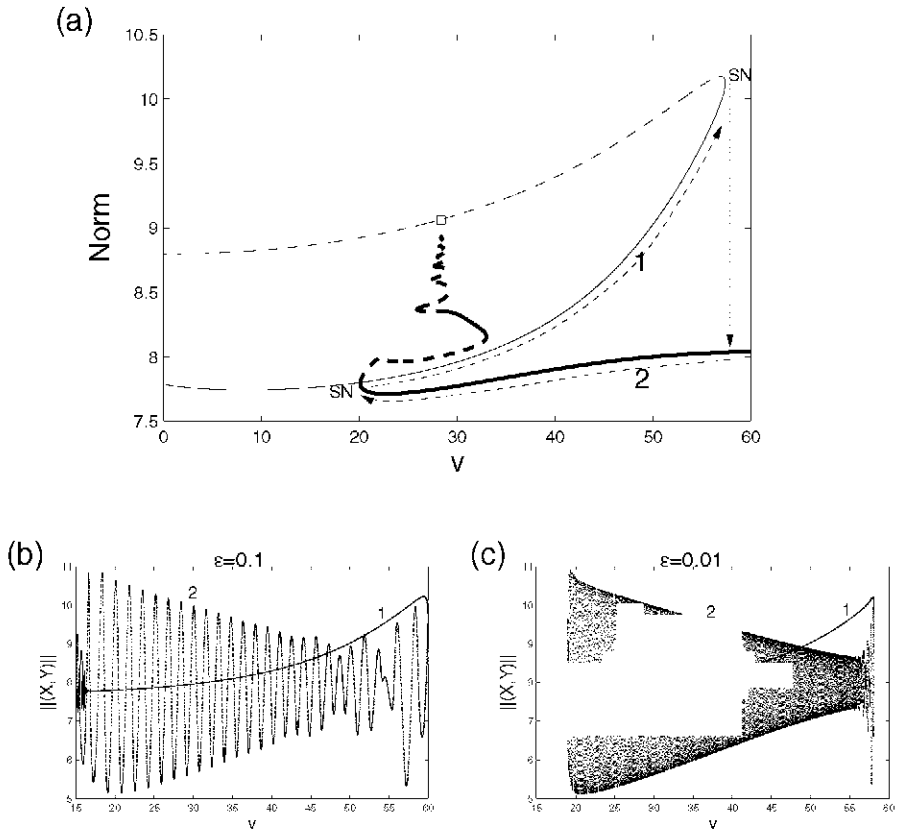

Figure 19. Stable periodic relaxation oscillations for $\Gamma = -7.5$, $\mu = 6.0$. (a) The fast system ($\varepsilon = 0$) projected on the $(||(X,Y)||_{L^2}, v)$ plane. Thick solid (dashed) lines indicate branches of stable (unstable) oscillations, while thin solid (dashed) lines indicate stable (unstable) steady states. The oscillations terminate in a heteroclinic bifurcation of Shil'nikov type (indicated by $\square$). The slow drifts, present when $0 < \varepsilon \ll 1$, are labeled with integers to indicate the corresponding phase in the solutions computed from Eqs. (19) with (b) $\varepsilon = 0.1$ and (c) $\varepsilon = 0.01$. The arrows in (a) indicate the direction of drift as well as the location of the fast transitions.

3.3. Relaxation oscillations near onset

In the preceding section we located chaotic dynamics between the codimension-two points TB and SN/H on the P_+ branch (Fig. 11(a)), i.e., for positive detuning Γ. In contrast, for negative detuning we find *relaxation* oscillations involving both steady and periodic orbits; these are associated with the TB bifurcation on the P_- branch (Fig. 11(a)) since it is this bifurcation that is responsible for the appearance of oscillations in this regime. The relaxation oscillations are found for $-11 \lesssim \Gamma \lesssim -3$, the values of Γ used in [19] (see figure 9 of their paper).

Figure 19(a) shows a projection onto the $(||(X,Y)||_{L_2}, v)$ plane of the steady and periodic solutions of the fast system, obtained from Eqs. (19) by setting $\varepsilon \quad 0$. As in the case of the elliptical domain the fast system admits both steady and periodic solutions, with the periodic oscillations terminating in a heteroclinic bifurcation on the unstable steady states U. However, there is an important difference between these two cases. In the elliptical case (Sect. 2.3) the leading stable and unstable eigenvalues $-\lambda_s \pm i\omega$, λ_u of U at the global bifurcation satisfy the condition $\delta \equiv \lambda_s/\lambda_u > 1$, implying that the periodic oscillations approach the global bifurcation monotonically, and remain stable throughout. In the present case the leading eigenvalues are $\lambda_u \quad 10.2737$, $\lambda_s \pm i\omega \quad -0.999548 \pm 19.89559i$ implying that $\delta < 1$. Consequently the branch of periodic oscillations undergoes an infinite number of back-

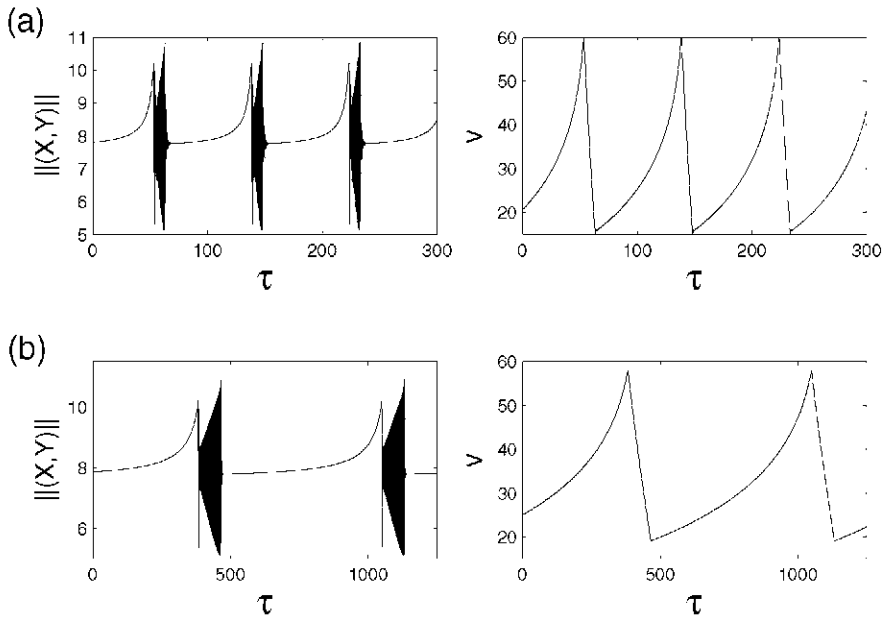

Figure 20. Time series corresponding to the attractors in Fig. 19(b,c). (a) $\epsilon = 0.1$ and (b) $\epsilon = 0.01$.

and-forth oscillations as it approaches the global bifurcation (see Fig. 19(a)). In this region one finds multiple coexisting stable oscillations, as described, for example, by Glendinning and Sparrow [5]. Intervals of stable oscillations are created and destroyed at saddle-node bifurcations; within each such interval near the global bifurcation there are cascades of period-doubling bifurcations leading to intervals of chaos. Subsidiary (multipulse) heteroclinic orbits are also present. However, despite this increased complexity in the behavior of the fast system the relaxation oscillations that take place once $\varepsilon > 0$ are relatively simple. This is because the slow drift along the branch of periodic oscillations (labeled 2 in Fig. 19(a)) takes the system to the first sadddle-node bifurcation, where the system jumps to the stable steady state S of the fast system; thereafter it drifts along S towards larger v (labeled 1 in Fig. 19(a)) and hence towards the saddle-node bifurcation on S where an abrupt transition back to periodic oscillations takes place. The resulting relaxation oscillations are shown in Figs. 19(b,c) for two values of ε.

Since the drift along the branch of periodic solutions of the fast system now terminates at a saddle-node bifurcation the trajectory drifts past the saddle-node bifurcation and approaches the stable steady states S of the fast system *without* visiting a neighborhood of the unstable states U. It is for this reason that the relaxation oscillations in the rectangular domain take a *simpler* form than those in the elliptical domain. In the latter the eigenvalues of U control the reinjection of the trajectory to one of a pair of S, a fact that is responsible for the succession of transitions between relaxation oscillations of different symmetry types. Moreover, the close approach to U is also responsible for the observed drifts along U. In contrast, any drifts along U in Eqs. (19) would be a consequence of a *canard*, and consequently would be restricted to an exponentially small interval in μ as $\varepsilon \to 0$.

4. Discussion

In this paper we have examined the dynamics of parametrically driven Faraday waves in three-dimensional containers on the assumption that (i) the viscosity of the liquid is small (as measured by the dimensionless quantity $C_g \ll 1$) and (ii) the effective Reynolds number of the streaming

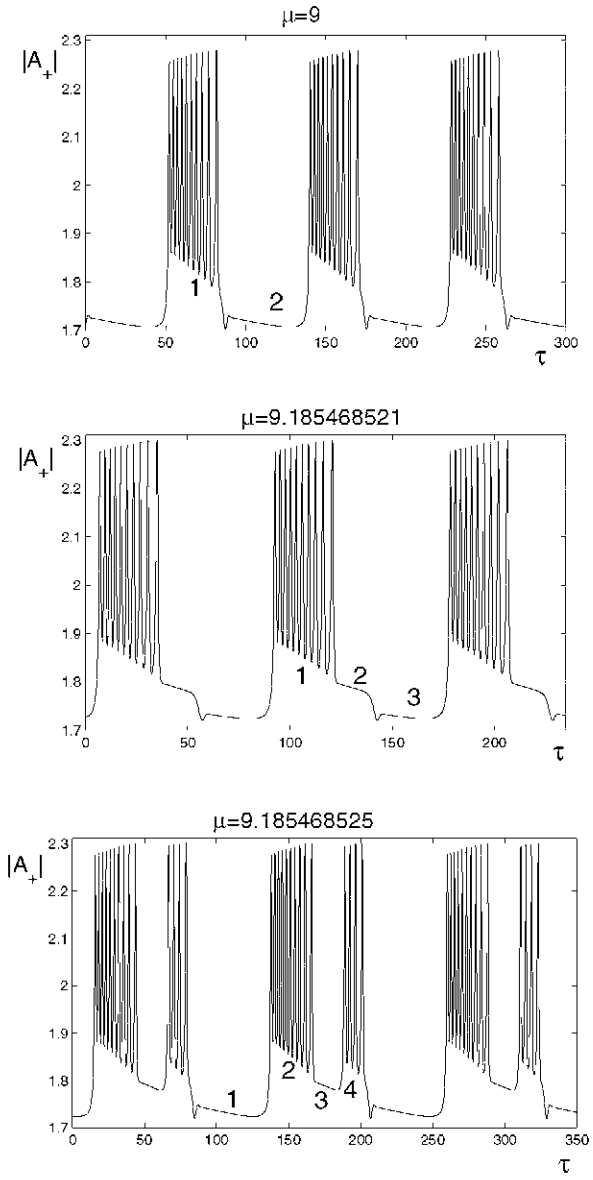

Figure 21. (a) The time series of Fig. 9(a) replotted in terms of the rotating wave amplitudes $A_{\pm}$, revealing a sequence of Type Ia bursts reminiscent of pancreatic β-cells. The labels 1 and 2 indicate the two slow phases, a drift along a branch of steady states and of periodic orbits of the fast system, respectively. Figures (b,c) correspond to Figs. 9(b,c).

flow driven in oscillatory boundary layers is also small. We focused on the role of forced symmetry breaking in providing a coupling between the streaming flow and the oscillations responsible for the oscillatory boundary layers driving this flow. As examples we have chosen (a) a container with a circular cross-section perturbed into an elliptical one, and (b) a square container perturbed into a slightly rectangular one. Both systems are described by a five-dimensional system of ordinary differential equations with the symmetry D_2 of a rectangle. These equations are almost identical; it is not surprising therefore that they exhibit similar dynamics. We have focused on an unexpected property of these equations, namely relaxation oscillations. These oscillations consist of slow phases interrupted by fast 'jumps' from one state to another, and are possible because of the disparity in

time scales for the decay of free surface gravity-capillary waves and of the streaming flow. When $C_g \ll 1$ the latter decays much more slowly, a fact that is responsible for the singular perturbation structure of our reduced system. In both cases the fast system, obtained by freezing the streaming flow, exhibited both steady states and periodic oscillations; as a result we were able to find in the slow-fast system relaxation oscillations consisting of slow drifts along (slow) manifolds of steady states and periodic orbits with fast 'jumps' between them. These jumps are typically triggered by the passage through a saddle-node bifurcation, although in case (a) a global bifurcation of the periodic states plays a similar role. The reason this is so is that the leading eigenvalues at the global bifurcation satisfy the inequality $\delta > 1$. In contrast, the eigenvalues in case (b) satisfy the Shil'nikov inequality $\delta < 1$ with the result that the drift along the manifold of periodic orbits 'misses' the global bifurcation. The consequences of this difference are profound. In case (a) the trajectory of the system is forced into a neighborhood of the unstable states. As a consequence the system drifts for a time along these unstable states before following the unstable manifold to one of a pair of symmetry-related stable steady states. It is this feature of the system that is responsible for the rich dynamics described in Sect. 2.3. In contrast, in case (b) the trajectory avoids the unstable steady states entirely and the dynamics is much more conventional.

In both cases we have used the coefficients of the nonlinear terms computed from inviscid theory, and estimates of the decay rates of the surface gravity-capillary waves and of the streaming flow, and explored the dependence of the system on the forcing amplitude and frequency (i.e., detuning) for fixed symmetry breaking as measured by the parameter Λ. Thus except for the unknown value of the coefficient γ that describes the coupling of the surface waves to the streaming flow all the coefficient values used represent realistic values. However, despite this effort, we have not been able to reproduce in detail the relaxation oscillations reported by Simonelli and Gollub in [19].

We conclude by noting that if the time series (Fig. 9a) is replotted using the rotating wave amplitudes $A_\pm$ (Fig. 21a) the result is indistinguishable from the so-called type Ia bursts exhibited, for example, by pancreatic β-cells [9], and indeed the dynamical systems explanation of this behavior suggested in Sect. 2.3 has much in common with that advanced for pancreatic β-cells by Terman [20]. There is one key difference, however, in addition to the absence of symmetry. In the pancreatic β-cell model Terman assumes that the slow drift along U is in the *same* direction as that along the periodic states p; in our problem these drifts are in opposite directions, and it is this fact that is responsible for the dramatic oscillations shown in Fig. 9(b,c), see also Fig. 10, and replotted in Fig. 21(b,c).

Acknowledgments

Acknowledgments This work was supported in part by a NASA Microgravity Sciences Grant NNC04GA47G. We are grateful to Drs J. Moehlis and J. Porter for numerous discussions.

References

[1] Armbruster D, Guckenheimer J and Kim S 1991 *Resonant Surface Waves in a Square Container* (Differential Equations and Computer Algebra) ed M Singer (New York: Academic Press) pp 61–76

[2] Batiste O and Knobloch E 2005 Simulations of oscillatory convection in ^{3}He-^{4}He mixtures in moderate aspect ratio containers *Phys. Fluids* **17** 064102

[3] Douady S, Fauve S and Thual O 1989 Oscillatory phase modulation of parametrically forced surface waves *Europhys. Lett.* **10** 309

[4] Feng Z C and Sethna P R 1989 Symmetry-breaking bifurcations in resonant surface waves *J. Fluid Mech.* **199** 495

[5] Glendinning P and Sparrow C 1984 Local and global behavior near homoclinic orbits *J Stat. Phys.* **35** 645

[6] Higuera M, Knobloch E and Vega J M 2005 Dynamics of nearly inviscid Faraday waves in almost circular containers *Physica D* **201** 83

[7] Higuera M, Porter J and Knobloch E 2002 Heteroclinic dynamics in the nonlocal parametrically driven nonlinear Schrödinger equation *Physica D* **162** 155

[8] Iliguera M, Vega J M and Knobloch E 2002 Coupled amplitude-streaming flow equations for nearly inviscid Faraday waves in small aspect ratio containers *J. Nonlin. Sci.* **12** 505
[9] Keener J and Sneyd J 1998 *Mathematical Physiology* (New York: Springer-Verlag)
[10] Knobloch E and Cuckenheimer J 1983 Convective transitions induced by a varying aspect ratio *Phys. Rev.* A **27** 408
[11] Landsberg A S and Knobloch E 1991 Direction-reversing traveling waves *Phys. Lett.* A **159** 17
[12] Longuet-Higgins M S 1953 Mass transport in water waves *Phil. Trans. R. Soc.* A **245** 535
[13] Martel C, Nicolás J A and Vega J M 1998 Surface-wave damping in a brimful circular cylinder *J. Fluid Mech.* **360** 213
[14] Martín E, Martel C and Vega J M 2002 Drift instability of standing Faraday waves *J. Fluid Mech.* **467** 57
[15] Miles J W 1984 Internally resonant surface waves in a circular cylinder *J. Fluid Mech.* **149** 1
[16] Mochlis J and Knobloch E 1998 Forced symmetry breaking as a mechanism for bursting *Phys. Rev. Lett.* **80** 5329
[17] Schlichting H 1932 Berechnung ebener periodischer Grenzschichtströmungen *Phys. Z.* **33** 327
[18] Silber M and Knobloch E 1989 Parametrically excited surface waves in square geometry *Phys. Lett.* A **137** 349
[19] Simonelli F and Gollub J P 1989 Surface wave mode interactions: effects of symmetry and degeneracy *J. Fluid Mech.* **199** 471
[20] Terman D 1991 Chaotic spikes arising from a model of bursting in excitable membranes *SIAM J. Appl. Math.* **51** 1418
[21] Vega J M, Knobloch E and Martel C 2001 Nearly inviscid Faraday waves in annular containers of moderately large aspect ratio *Physica D* **154** 313